

Highly efficient energy-conserving moment method for the multi-dimensional Vlasov-Maxwell system

Tianai Yin*, Xinghui Zhong[†], Yanli Wang[‡]

June 1, 2022

Abstract

In this paper, we propose an energy-conserving numerical method to solve the Vlasov-Maxwell (VM) system based on the regularized moment method proposed in [4]. The globally hyperbolic moment system is deduced for the multi-dimensional VM system under the framework of the Hermite expansions, where the expansion center and the scaling factor are set as the macroscopic velocity and local temperature, respectively. Thus, the effect of the Lorentz force term can be reduced into several ODEs about the macroscopic velocity and the moment coefficients of higher order, which could significantly reduce the computational cost of the whole system. An energy-conserving numerical scheme is proposed to solve the moment equations and Maxwell's equations, where only a linear equation system needs to be solved. Several numerical examples such as the two-stream instability, Weibel instability, and the two-dimensional Orszag-Tang vortex problem are studied to validate the efficiency and excellent energy-preserving property of the numerical scheme.

Keywords: Vlasov-Maxwell system; regularized moment method; energy conservation

1 Introduction

Plasma, which exists widely in the universe, is the fourth fundamental state of matter after solid, liquid, and gas. Understanding the complex behavior of plasma has led to significant advances ranging from space physics and fusion energy, to high-power microwave generation and large-scale particle accelerators. One of the fundamental models in plasma physics is the Vlasov system [2], which describes the time evolution of the distribution function of collisionless charged particles with long-range interactions. The long-range interactions may occur under a self-generated electromagnetic field. For example, the evolution of the electromagnetic field can be modeled by Maxwell's equations or Poisson's equation in the zero-magnetic field limit, resulting in the well-known Vlasov-Maxwell (VM) or Vlasov-Poisson (VP) systems.

Numerically solving the VM system is a difficult task. There are several challenges such as the non-ignorable high dimensionality, the conservation of physical quantities due to the Hamiltonian structure of the system [28, 29], various physical phenomena, nonlinearity, etc. Generally, there are two types of methods, i.e. stochastic methods and deterministic methods. Among the stochastic methods, the particle-in-cell (PIC) method [13, 38, 1] has been a prevalent numerical tool for a long time. In the PIC method, each plasma particle is considered, and all macro-quantities are calculated from the position and velocity of these particles. Meanwhile, the force acting on the particles is calculated from the field equations. The PIC method enjoys

*Beijing Computational Science Research Center, Beijing, 100193, China. Email: tianai.yin@csrc.ac.cn

[†]School of Mathematical Sciences, Zhejiang University, Hangzhou, 310027, China. Email: zhongxh@zju.edu.cn

[‡]Beijing Computational Science Research Center, Beijing, 100193, China. Email: ylwang@csrc.ac.cn

the advantage of a relatively low cost for high-dimensional problems and the accurate calculation of the convection term due to the Lagrangian nature, while suffering from the statistical noise and low resolution of the electron distribution function, especially when dealing with low temperature and high densities plasma [15]. In addition, several works have been done for PIC to preserve physical conservation. The method in [1] can only conserve mass and momentum in a uniform computational grid. In [24, 18], the time-explicit energy-conserving schemes are presented. Moreover, the energy-conserving implicit PIC algorithms for the VM system with a finite difference method in the physical space are proposed in [27], while a fully implicit solver for the VA system based on Newton-Krylov methods is proposed in [8]. Recently, a highly efficient UGKWP method, combined with the deterministic UGKS method and the stochastic Monte Carlo method, has been proposed to solve the Boltzmann equations and then extended to the VM system [25].

For the deterministic methods, there are also several different types of solvers. For example, the Runge-Kutta discontinuous Galerkin methods (RKDG) have been proposed in [11] for the VP and VM system. Semi-Lagrangian methods [7, 6, 33, 35], which are also combined with WENO reconstruction [41] or DG methods [3], are adopted to solve Vlasov-type equations. Moreover, the spectral methods, where the Fourier basis function or the Hermite polynomials are utilized to approximate the distribution functions, have been widely studied. We refer to [21, 17] and the references therein for more details. Besides, the finite difference method [39] and Hamiltonian splitting method [12] all have specific solvers for the VM system. For most of the methods proposed above, the conservation of the number of particles is easy to achieve, while the conservation of the total energy will be much more difficult. Achieving energy conservation is also a developing goal of the above methods. The implicit and explicit energy-preserving RKDG methods have been proposed in [10, 9] for the Vlasov-Ampère (VA) and VM systems, respectively. In the Hermite-DG method [31], the total energy is conserved when the central numerical fluxes are employed with Maxwell's equations solved by the DG method. In [16], a dynamical low-rank algorithm that conserves mass, momentum, and energy, is proposed for the VP system.

Recently, a regularized moment method has been presented for the kinetic equation, where a series of Hermite expansions are adopted to approximate the distribution function [4], where the expansion center and the scaling factor of the basis functions are set as the macroscopic velocity and the local temperature, respectively, which are chosen adaptively according to the distribution function. Moreover, a special regularization method is proposed to obtain the globally hyperbolic moment systems for kinetic equations [4]. This regularized moment method naturally bridges between the macroscopic and microscopic descriptions of the particles. It has been verified that this method has spectral convergence with the number of moments, and has been successfully applied to solve the Boltzmann-type equations [4], the VP system [5], and the 1D VPFP equations numerically [40].

Though it is verified to be efficient, the numerical schemes adopted in [5] can only preserve the conservation of mass and momentum for the VP system, and no results on the conservation of the total energy have been achieved. Inspired by the efficiency of the regularized moment method and the energy-conserving RKDG method in [10, 9], we propose an energy-conserving regularized moment method for the multi-dimensional VM system. The distribution function is expanded by a series of Hermite functions, with the expansion center and the scaling factor chosen adaptively as in [5]. With this specially chosen expansion center, the effect of the Lorentz force from the electromagnetic field can be changed into a linear combination of the moment coefficients, in which case the computational cost can be significantly reduced. To design the energy-conserving scheme, the moment system is split into the convection step and the Lorentz force step by the Strang-splitting method. Thus, the effect of the Lorentz force term is reduced to several ODEs on the macroscopic velocity and high-order moment coefficients. Most importantly, an implicit scheme is developed to solve Maxwell's equations and Lorentz force step

simultaneously, enabling the exact conservation of mass and total energy for the VM system. Only a very small system of linear equations needs to be solved for this implicit scheme. Several numerical examples of the VM system, such as the one-dimensional Landau damping, two-stream instability, Weibel instability, and the two-dimensional Orszag-Tang vortex problems, are studied to exhibit the high efficiency of this energy-conserving numerical method.

The rest of the paper is as follows: the VM system and related physical properties are introduced briefly in Sec. 2. The regularized moment method and the deduction of the globally hyperbolic moment equations are proposed in Sec. 3. In Sec. 4, the semi-discrete and fully discrete energy-conserving numerical schemes are presented with the related proof. Several numerical tests are studied in Sec. 5, with some concluding remarks in Sec. 6.

2 The Vlasov-Maxwell equations

In this section, we introduce the VM system. Under suitable scaling of the characteristic time, the length, and the characteristic electric and magnetic field, the dimensionless Vlasov equation is given by

$$\frac{\partial f}{\partial t} + \mathbf{v} \cdot \nabla_{\mathbf{x}} f + (\mathbf{E} + \mathbf{v} \times \mathbf{B}) \cdot \nabla_{\mathbf{v}} f = 0, \quad (t, \mathbf{x}, \mathbf{v}) \in \mathbb{R}^+ \times \Omega \times \mathbb{R}^3, \quad (2.1)$$

where $f(t, \mathbf{x}, \mathbf{v})$ is the distribution function describing the motion of the charged particles at position \mathbf{x} with microscopic velocity \mathbf{v} at time t . $\Omega \subset \mathbb{R}^3$ denotes the spatial domain, while \mathbb{R}^3 denotes the 3-dimensional microscopic velocity space. (\mathbf{E}, \mathbf{B}) is the electromagnetic field, when it is modeled by the dimensionless Maxwell's equations

$$\begin{cases} \frac{\partial \mathbf{E}}{\partial t} - \nabla_{\mathbf{x}} \times \mathbf{B} = -\mathbf{J}, \\ \frac{\partial \mathbf{B}}{\partial t} + \nabla_{\mathbf{x}} \times \mathbf{E} = 0, \end{cases} \quad (2.2)$$

with the current density \mathbf{J} defined as

$$\mathbf{J}(t, \mathbf{x}) = \int_{\mathbb{R}^3} \mathbf{v} f(t, \mathbf{x}, \mathbf{v}) d\mathbf{v}, \quad (2.3)$$

we obtain the Vlasov-Maxwell system. It is worth mentioning that Maxwell's equations (2.2) are further supplemented by Gauss's law [19] as

$$\nabla_{\mathbf{x}} \cdot \mathbf{E} = \rho - \rho_{\text{bound}}, \quad \nabla_{\mathbf{x}} \cdot \mathbf{B} = 0, \quad (2.4)$$

with the density ρ defined as

$$\rho = \int_{\mathbb{R}^3} f(t, \mathbf{x}, \mathbf{v}) d\mathbf{x}, \quad (2.5)$$

and ρ_{bound} being the density of particles from the background. When the background is vacuum, $\rho_{\text{bound}} = 0$. In the zero-magnetic limit, the VM system becomes the VP or VA system

$$\begin{aligned} \frac{\partial f}{\partial t} + \mathbf{v} \cdot \nabla_{\mathbf{x}} f + \mathbf{E} \cdot \nabla_{\mathbf{v}} f &= 0, \\ \mathbf{E} &= -\nabla \phi, \quad -\Delta \phi = \rho - \rho_{\text{bound}}, \quad \text{Vlasov-Poisson}, \\ \frac{\partial \mathbf{E}}{\partial t} &= -\mathbf{J}, \quad \text{Vlasov-Ampère}. \end{aligned} \quad (2.6)$$

The VP and VA systems are equivalent in the absence of external fields, when the charge continuity equation

$$\frac{\partial \rho}{\partial t} + \nabla_{\mathbf{x}} \cdot \mathbf{J} = 0$$

is satisfied.

In this paper, we focus on the VM system. All the discussions can be extended to the VA system by properly adjusting $\mathbf{B} = 0$. Besides, the density ρ defined in (2.5), we are also interested in the physical variables such as the macroscopic velocity \mathbf{u} and the thermal temperature \mathcal{T} satisfying

$$\rho \mathbf{u} = \int_{\mathbb{R}^3} \mathbf{v} f \, d\mathbf{v}, \quad \frac{1}{2} \rho |\mathbf{u}|^2 + \frac{3}{2} \rho \mathcal{T} = \frac{1}{2} \int_{\mathbb{R}^3} |\mathbf{v}|^2 f \, d\mathbf{v}, \quad (2.7)$$

as well as the heat flux \mathbf{q} and the pressure tensor p_{ij} defined as

$$\mathbf{q} = \frac{1}{2} \int_{\mathbb{R}^3} |\mathbf{v} - \mathbf{u}|^2 (\mathbf{v} - \mathbf{u}) f \, d\mathbf{v}, \quad p_{ij} = \int_{\mathbb{R}^3} (v_i - u_i)(v_j - u_j) f \, d\mathbf{v}, \quad i, j = 1, 2, 3. \quad (2.8)$$

More details can be found in [37].

For a collision-based system composed with a large number of non-interacting particles, where quantum effects can be ignored, the most likely distribution function [22] is the Maxwellian distribution, which is also known as the equilibrium distribution, defined as

$$f_{\text{eq}}(t, \mathbf{x}, \mathbf{v}) = \frac{\rho(t, \mathbf{x})}{[2\pi\mathcal{T}(t, \mathbf{x})]^{3/2}} \exp\left(-\frac{(\mathbf{v} - \mathbf{u}(t, \mathbf{x}))^2}{2\mathcal{T}(t, \mathbf{x})}\right). \quad (2.9)$$

Moreover, the VM system conserves the total particle number $\mathcal{P}(t)$ and the total energy $\mathcal{E}_{\text{total}}(t)$, defined as

$$\mathcal{P}(t) = \int_{\Omega \times \mathbb{R}^3} f(t, \mathbf{x}, \mathbf{v}) \, d\mathbf{x} \, d\mathbf{v}, \quad \mathcal{E}_{\text{total}}(t) = \mathcal{E}_K(t) + \mathcal{E}_B(t) + \mathcal{E}_E(t), \quad (2.10a)$$

where $\mathcal{E}_{\text{total}}(t)$ is composed of the kinetic and electromagnetic energy as

$$\begin{aligned} \mathcal{E}_K(t) &= \frac{1}{2} \int_{\Omega} \int_{\mathbb{R}^3} |\mathbf{v}|^2 f(t, \mathbf{x}, \mathbf{v}) \, d\mathbf{v} \, d\mathbf{x} = \frac{1}{2} \int_{\Omega} \rho |\mathbf{u}|^2 + 3\rho \mathcal{T} \, d\mathbf{x}, \\ \mathcal{E}_E(t) &= \frac{1}{2} \int_{\Omega} |\mathbf{E}(t, \mathbf{x})|^2 \, d\mathbf{x}, \quad \mathcal{E}_B(t) = \frac{1}{2} \int_{\Omega} |\mathbf{B}(t, \mathbf{x})|^2 \, d\mathbf{x}. \end{aligned} \quad (2.11)$$

3 The moment method

In this section, we lay out the details of the moment method for the VM system, to obtain the moment equations of the VM system and discuss their hyperbolicity property.

3.1 Series expansion and moment systems

Following the method in [?, ?, 5], the distribution function $f(t, \mathbf{x}, \mathbf{v})$ is expanded into Hermite series as

$$f(t, \mathbf{x}, \mathbf{v}) = \sum_{\alpha \in \mathbb{N}^3} f_{\alpha}(t, \mathbf{x}) \mathcal{H}_{\mathcal{T}, \alpha} \left(\frac{\mathbf{v} - \mathbf{u}(t, \mathbf{x})}{\sqrt{\mathcal{T}(t, \mathbf{x})}} \right), \quad (3.1)$$

where the basis functions $\mathcal{H}_{\mathcal{T}, \alpha}(\cdot)$ are defined as

$$\mathcal{H}_{\mathcal{T}, \alpha}(\boldsymbol{\xi}) = \frac{1}{(2\pi)^{3/2}} \mathcal{T}^{-\frac{|\alpha|+3}{2}} \prod_{d=1}^3 H_{\alpha_d}(\xi_d) \exp\left(-\frac{\xi_d^2}{2}\right). \quad (3.2)$$

Here $\alpha = (\alpha_1, \alpha_2, \alpha_3)$ is a 3-dimensional multi-index, $\boldsymbol{\xi} = (\xi_1, \xi_2, \xi_3)$ is defined as

$$\boldsymbol{\xi} = \frac{\mathbf{v} - \mathbf{u}(t, \mathbf{x})}{\sqrt{\mathcal{T}(t, \mathbf{x})}}, \quad (3.3)$$

and H_{α_d} is the Hermite polynomial

$$H_k(x) = (-1)^k \exp\left(\frac{x^2}{2}\right) \frac{d^k}{dx^k} \exp\left(-\frac{x^2}{2}\right). \quad (3.4)$$

For convenience, $H_k(x)$ is taken as zero if $k < 0$. Thus, $\mathcal{H}_{\mathcal{T},\alpha}$ is zero when any component of α is negative. Hermite polynomials have several important properties, which are useful for deriving the moment equations of the VM system, such as

- Orthogonality:

$$\int_{\mathbb{R}} H_m(x) H_k(x) \exp\left(\frac{-x^2}{2}\right) dx = m! \sqrt{2\pi} \delta_{mk}, \quad (3.5)$$

- Recursion relation:

$$H_{k+1}(x) = xH_k(x) - kH_{k-1}(x), \quad (3.6)$$

- Differential relation:

$$H'_k(x) = kH_{k-1}(x). \quad (3.7)$$

With the orthogonality of the Hermite polynomials, the moment coefficients f_α in (3.1) satisfy

$$\rho = f_0, \quad f_{e_i} = 0, \quad i = 1, 2, 3, \quad \sum_{d=1}^3 f_{2e_d} = 0, \quad (3.8)$$

$$q_i = 2f_{3e_i} + \sum_{d=1}^3 f_{2e_d+e_i}, \quad p_{ij} = \delta_{ij}\rho\mathcal{T} + (1 + \delta_{ij})f_{e_i+e_j}, \quad i, j = 1, 2, 3, \quad (3.9)$$

where e_d is the 3-dimensional multi-index whose d -th entry is 1 and all other entries are zero. Moreover, based on the properties of the Hermite polynomials, it holds for the basis functions $\mathcal{H}_{\mathcal{T},\alpha}$ that

$$\frac{\partial}{\partial v_j} \mathcal{H}_{\mathcal{T},\alpha} \left(\frac{\mathbf{v} - \mathbf{u}}{\sqrt{\mathcal{T}}} \right) = -\mathcal{H}_{\mathcal{T},\alpha+e_j} \left(\frac{\mathbf{v} - \mathbf{u}}{\sqrt{\mathcal{T}}} \right), \quad (3.10)$$

$$v_j \mathcal{H}_{\mathcal{T},\alpha} \left(\frac{\mathbf{v} - \mathbf{u}}{\sqrt{\mathcal{T}}} \right) = \mathcal{T} \mathcal{H}_{\mathcal{T},\alpha+e_j} + u_j \mathcal{H}_{\mathcal{T},\alpha} + \alpha_j \mathcal{H}_{\mathcal{T},\alpha-e_j}, \quad j = 1, 2, 3. \quad (3.11)$$

Thus, the force term $(\mathbf{E} + \mathbf{v} \times \mathbf{B}) \cdot \nabla_{\mathbf{v}} f$ is expanded as

$$\begin{aligned} & (\mathbf{E} + \mathbf{v} \times \mathbf{B}) \cdot \nabla_{\mathbf{v}} f \\ &= - \sum_{\alpha \in \mathbb{N}^3} \left\{ \sum_{d,l,m=1}^3 \left[(E_d + \epsilon_{dlm} u_l B_m) f_{\alpha-e_d} + \epsilon_{dlm} (\alpha_l + 1) B_m f_{\alpha-e_d+e_l} \right] \right\} \mathcal{H}_{\mathcal{T},\alpha} \left(\frac{\mathbf{v} - \mathbf{u}}{\sqrt{\mathcal{T}}} \right), \end{aligned} \quad (3.12)$$

where ϵ_{dlm} are the Levi-Civita symbols defined as

$$\epsilon_{dlm} = \begin{cases} 1, & \text{if } (d, l, m) \text{ is a cyclic permutation of } (1, 2, 3), \\ -1, & \text{if } (d, l, m) \text{ is an anticyclic permutation of } (1, 2, 3), \\ 0, & \text{if } (d-l)(l-m)(m-d) = 0. \end{cases} \quad (3.13)$$

Substituting (3.1) into the Vlasov equation (2.1), and matching the coefficients on both sides, the moment system for the Vlasov equation is derived as

$$\begin{aligned}
& \frac{\partial f_\alpha}{\partial t} + \sum_{d=1}^3 \left(\frac{\partial u_d}{\partial t} + \sum_{j=1}^3 u_j \frac{\partial u_d}{\partial x_j} - E_d - \sum_{l,m=1}^3 \epsilon_{dlm} u_l B_m \right) f_{\alpha-e_d} \\
& - \sum_{d,l,m=1}^3 \epsilon_{dlm} (\alpha_l + 1) B_m f_{\alpha-e_d+e_l} + \frac{1}{2} \left(\frac{\partial \mathcal{T}}{\partial t} + \sum_{j=1}^3 u_j \frac{\partial \mathcal{T}}{\partial x_j} \right) \sum_{d=1}^3 f_{\alpha-2e_d} \\
& + \sum_{d,j=1}^3 \left[\frac{\partial u_d}{\partial x_j} (\mathcal{T} f_{\alpha-e_d-e_j} + (\alpha_j + 1) f_{\alpha-e_d+e_j}) + \frac{1}{2} \frac{\partial \mathcal{T}}{\partial x_j} (\mathcal{T} f_{\alpha-2e_d-e_j} + (\alpha_j + 1) f_{\alpha-2e_d+e_j}) \right] \\
& + \sum_{j=1}^3 \left(\mathcal{T} \frac{\partial f_{\alpha-e_j}}{\partial x_j} + u_j \frac{\partial f_\alpha}{\partial x_j} + (\alpha_j + 1) \frac{\partial f_{\alpha+e_j}}{\partial x_j} \right) = 0, \quad \forall |\alpha| \geq 0.
\end{aligned} \tag{3.14}$$

Following the routine in [5], we can deduce the equations for the density, macroscopic velocity and temperature from (3.14) by letting $\alpha = \mathbf{0}$, e_d and $2e_d$, $d = 1, 2, 3$, as

$$\begin{aligned}
& \frac{\partial \rho}{\partial t} + \sum_{j=1}^3 \left(u_j \frac{\partial \rho}{\partial x_j} + \rho \frac{\partial u_j}{\partial x_j} \right) = 0, \\
& \frac{\partial u_d}{\partial t} + \sum_{j=1}^3 u_j \frac{\partial u_d}{\partial x_j} + \frac{1}{\rho} \sum_{j=1}^3 \frac{\partial p_{jd}}{\partial x_j} = E_d + \sum_{l,m=1}^3 \epsilon_{dlm} u_l B_m, \\
& \rho \left(\frac{\partial \mathcal{T}}{\partial t} + \sum_{j=1}^3 u_j \frac{\partial \mathcal{T}}{\partial x_j} \right) + \frac{2}{3} \sum_{j=1}^3 \left(\frac{\partial q_j}{\partial x_j} + \sum_{d=1}^3 p_{jd} \frac{\partial u_d}{\partial x_j} \right) = 0.
\end{aligned} \tag{3.15}$$

Moreover, substituting (3.15) into (3.14) to eliminate the terms with temporal derivatives of u_d and \mathcal{T} , it holds for the high order moment coefficients that

$$\begin{aligned}
& \frac{\partial f_\alpha}{\partial t} + \sum_{j=1}^3 \left(\mathcal{T} \frac{\partial f_{\alpha-e_j}}{\partial x_j} + u_j \frac{\partial f_\alpha}{\partial x_j} + (\alpha_j + 1) \frac{\partial f_{\alpha+e_j}}{\partial x_j} \right) \\
& + \sum_{d,j=1}^3 \left[\mathcal{T} f_{\alpha-e_d-e_j} + (\alpha_j + 1) f_{\alpha-e_d+e_j} - \frac{p_{jd}}{3\rho} \sum_{l=1}^3 f_{\alpha-2e_l} \right] \frac{\partial u_d}{\partial x_j} \\
& - \sum_{d,j=1}^3 \frac{f_{\alpha-e_d}}{\rho} \frac{\partial p_{jd}}{\partial x_j} - \frac{1}{3\rho} \left(\sum_{k=1}^3 f_{\alpha-2e_k} \right) \sum_{j=1}^3 \frac{\partial q_j}{\partial x_j} \\
& + \sum_{j=1}^3 \left[\sum_{d=1}^3 \mathcal{T} f_{\alpha-2e_d-e_j} + (\alpha_j + 1) f_{\alpha-2e_d+e_j} \right] \left(-\frac{\mathcal{T}}{2\rho} \frac{\partial \rho}{\partial x_j} + \frac{1}{6\rho} \sum_{d=1}^3 \frac{\partial p_{dd}}{\partial x_j} \right) \\
& = \sum_{d,l,m=1}^3 \epsilon_{dlm} (\alpha_l + 1) B_m f_{\alpha-e_d+e_l}, \quad \forall |\alpha| \geq 2.
\end{aligned} \tag{3.16}$$

Collecting (3.15) and (3.16), we get the moment equations of the VM system with infinite number of equations. In the numerical simulation, a truncation should be adopted for the expansion of the distribution function in (3.1), rendering (3.16) a finite moment system. A regularization method is further applied to obtain a closed moment system, which we will discuss in the next section.

3.2 Closure of the moment system

To obtain a finite system, the expansion (3.1) is truncated as

$$f(t, \mathbf{x}, \mathbf{v}) \approx \sum_{|\alpha| \leq M} f_\alpha(t, \mathbf{x}) \mathcal{H}_{\mathcal{T}, \alpha} \left(\frac{\mathbf{v} - \mathbf{u}(t, \mathbf{x})}{\sqrt{\mathcal{T}(t, \mathbf{x})}} \right), \quad (3.17)$$

where M is the truncation order, and $|\alpha| = \alpha_1 + \alpha_2 + \alpha_3$. The resulted finite moment system is further closed by adopting the regularization proposed in [4]. Let $\mathbf{f} = (\rho, \mathbf{u}, \mathcal{T}, f_{2e_1}, \dots)$. Substituting the terms $f_\alpha, |\alpha| = M + 1$ with the regularized term in [4], the quasi-linear closed moment system can be rewritten as

$$\frac{\partial \mathbf{f}}{\partial t} + \sum_{j=1}^3 \hat{\mathbf{M}}_j(\mathbf{f}) \frac{\partial \mathbf{f}}{\partial x_j} = \mathbf{G} \mathbf{f} + \mathbf{g}, \quad (3.18)$$

with

$$\hat{\mathbf{M}}_j(\mathbf{f}) \frac{\partial \mathbf{f}}{\partial x_j} = \mathbf{M}_j(\mathbf{f}) \frac{\partial \mathbf{f}}{\partial x_j} - \sum_{|\alpha|=M} \mathcal{R}_M^j(\alpha) I_{\mathcal{N}(\alpha)}, \quad (3.19)$$

$$\mathcal{R}_M^j(\alpha) = (\alpha_j + 1) \left[\sum_{d=1}^D f_{\alpha - e_d + e_j} \frac{\partial u_d}{\partial x_j} + \frac{1}{2} \left(\sum_{d=1}^D f_{\alpha - 2e_d + e_j} \right) \frac{\partial \mathcal{T}}{\partial x_j} \right], \quad (3.20)$$

$$\mathbf{g}_{\mathcal{N}(e_i)} = E_i, \quad \mathbf{G}_{\mathcal{N}(\alpha), \mathcal{N}(\alpha - e_d + e_l)} = \sum_{m=1}^3 \epsilon_{dlm} (\alpha_l + 1) B_m, \quad d, l = 1, 2, 3, \quad (3.21)$$

where

$$\mathcal{N}(\alpha) = \sum_{i=1}^3 \left(\sum_{k=4-i}^3 \alpha_k + i - 1 \right) + 1. \quad (3.22)$$

Here \mathbf{M}_j is an $N \times N$ matrix with $N = C_{M+3}^3$, corresponding to the terms with derivatives of \mathbf{f} , the detailed form of which can be derived from the moment system (3.15) and (3.16). I_k is the k -th column of the $N \times N$ identity matrix. \mathbf{G} is an $N \times N$ matrix and \mathbf{g} is a vector of length N , whose entries are given in (3.21) while all other entries are zero. We refer readers to [4] for the detailed derivation of this moment system and the study on the global hyperbolicity of (3.18). We show here the most important result in the following lemma.

Lemma 1. *For any unit vector $\mathbf{n} = (n_1, n_2, n_3)^T \in \mathbb{R}^3$, the matrix $\sum_{j=1}^3 n_j \hat{\mathbf{M}}_j$ is diagonalizable. Precisely, its characteristic polynomial is*

$$\left| \lambda I - \sum_{j=1}^3 n_j \hat{\mathbf{M}}_j \right| = \prod_{i=0}^M \prod_{j=0}^i \mathcal{T}^{(j+1)/2} H_{j+1} \left(\frac{\lambda - \mathbf{u} \cdot \mathbf{n}}{\sqrt{\mathcal{T}}} \right), \quad (3.23)$$

and its eigenvalues are

$$\mathbf{u} \cdot \mathbf{n} + C_{i,j} \sqrt{\mathcal{T}}, \quad 1 \leq i \leq j \leq M + 1, \quad (3.24)$$

where $C_{i,j}$ is the i -th root of $H_j(z)$.

Up to now, we have obtained the closed moment equations for the VM system. It is worth mentioning that different from the VP system studied in [5], the magnetic field \mathbf{B} in the VM system is coupled in the governing equations of f_α . Thus, additional care needs to be taken to ensure the conservation properties. The energy-conserving numerical scheme will be introduced in the next section to solve the moment system coupling with Maxwell's equations (2.2).

4 Energy-conserving numerical schemes

In this section, we propose the energy-conserving numerical schemes for the VM system, with the temporal discrete schemes discussed in Sec. 4.1 and fully discrete schemes discussed in Sec. 4.2.

4.1 Temporal discrete schemes

Inspired by the numerical method for the VP system in [5], the Strang-splitting method is utilized to solve the VM system. Precisely, the Vlasov equation is split into the following two parts:

- the convection step

$$\frac{\partial f}{\partial t} + \mathbf{v} \cdot \nabla_{\mathbf{x}} f = 0, \quad (4.1)$$

- the Lorentz force step

$$\frac{\partial f}{\partial t} + (\mathbf{E} + \mathbf{v} \times \mathbf{B}) \cdot \nabla_{\mathbf{v}} f = 0. \quad (4.2)$$

In the framework of the regularized moment method discussed in Sec. 3, the governing equation (4.2) can be reduced into several ODEs based on (3.15) and (3.16), yielding

$$\frac{d\mathbf{u}}{dt} = \mathbf{E} + \mathbf{u} \times \mathbf{B}, \quad (4.3)$$

$$\frac{d\mathcal{T}}{dt} = 0, \quad (4.4)$$

$$\frac{df_{\alpha}}{dt} = \sum_{d,l,m=1}^3 \epsilon_{dlm} (\alpha_l + 1) B_m f_{\alpha - e_d + e_l}, \quad 2 \leq |\alpha| \leq M. \quad (4.5)$$

It is obvious the movement of particles subjected to the Lorentz force in the moment system is very concise. Moreover, compared to the general Hermite spectral method, it is surprised to find that (4.3) is Newton's first law of motion in classical mechanics. We also see that the high-order moment coefficients f_{α} are only related to the magnetic field and the moment coefficients in the same order of α . Although, there are few physical definitions of the high-order moment coefficients, we still expect more physical explanations for (4.5) in the future.

We now introduce two energy-conserving temporal schemes for (4.1) and (4.3)-(4.5) coupling with Maxwell's equations (2.2). As for the convection step (4.1), any implicit or explicit Runge-Kutta method can be applied to solve it and conserves the kinetic energy [9, 5]. We consider the forward Euler method for this step. The Lorentz step (4.3)-(4.5) and the Maxwell's equation (2.2) contain the main coupling of the macroscopic velocity and the electromagnetic field. Thus, the key point is how to advance the macroscopic velocity and the electromagnetic field in this step to balance the kinetic and electromagnetic energy.

For both schemes designed in the following, the electric field and the macroscopic velocity are advanced implicitly, while the magnetic field is advanced implicitly for one scheme and explicitly for the other. The first scheme, denoted by **Scheme-I**, is designed as follows

Scheme-I: Implicit for the magnetic field

$$\frac{f^{n+1,*} - f^n}{\Delta t} = -\mathbf{v} \cdot \nabla_{\mathbf{x}} f^n, \quad (4.6a)$$

$$\frac{\mathbf{B}^{n+1} - \mathbf{B}^n}{\Delta t} = -\nabla_{\mathbf{x}} \times \frac{\mathbf{E}^n + \mathbf{E}^{n+1}}{2}, \quad (4.6b)$$

$$\frac{\mathbf{E}^{n+1} - \mathbf{E}^n}{\Delta t} = \nabla_{\mathbf{x}} \times \frac{\mathbf{B}^n + \mathbf{B}^{n+1}}{2} - \mathbf{J}^{n+1/2}, \quad (4.6c)$$

$$\frac{\mathbf{u}^{n+1} - \mathbf{u}^{n+1,*}}{\Delta t} = \frac{\mathbf{E}^n + \mathbf{E}^{n+1}}{2} + \frac{\mathbf{u}^{n+1,*} + \mathbf{u}^{n+1}}{2} \times \frac{\mathbf{B}^n + \mathbf{B}^{n+1}}{2}, \quad (4.6d)$$

$$\frac{f_{\alpha}^{n+1} - f_{\alpha}^{n+1,*}}{\Delta t} = \sum_{d,l,m=1}^3 \epsilon_{dlm}(\alpha_l + 1) \frac{B_m^n + B_m^{n+1}}{2} f_{\alpha - e_d + e_l}^{n+1,*}, \quad 2 \leq |\alpha| \leq M. \quad (4.6e)$$

Here $\mathbf{J}^{n+1/2}$ is defined as

$$\mathbf{J}^{n+1/2} = \int_{\mathbb{R}^3} \mathbf{v} \left(\frac{f^{n+1,*} + f^{n+1}}{2} \right) d\mathbf{v} = \frac{\rho^{n+1} \mathbf{u}^{n+1} + \rho^{n+1,*} \mathbf{u}^{n+1,*}}{2}, \quad (4.7)$$

where $\rho^{n+1,*}$ and $\mathbf{u}^{n+1,*}$ are the density and the macroscopic velocity connected with $f^{n+1,*}$ in (4.6a) via (2.7). The density ρ and the thermal temperature \mathcal{T} remain unchanged during the Lorentz step, i.e.,

$$\rho^{n+1} = \rho^{n+1,*}, \quad \mathcal{T}^{n+1} = \mathcal{T}^{n+1,*}, \quad (4.8)$$

which renders (4.7) as

$$\mathbf{J}^{n+1/2} = \frac{\rho^{n+1,*}(\mathbf{u}^{n+1} + \mathbf{u}^{n+1,*})}{2}. \quad (4.9)$$

Theorem 1 (Total energy conservation of **Scheme-I**). **Scheme-I** preserves the discrete total energy

$$\mathcal{E}_{\text{total}}^{n+1} = \mathcal{E}_{\text{total}}^n, \quad (4.10)$$

for the VM system in Sec. 2 with periodic boundary conditions in \mathbf{x} , where

$$\mathcal{E}_{\text{total}}^n = \frac{1}{2} \int_{\Omega} \rho^n (|\mathbf{u}^n|^2 + 3\mathcal{T}^n) d\mathbf{x} + \frac{1}{2} \int_{\Omega} |\mathbf{E}^n|^2 + |\mathbf{B}^n|^2 d\mathbf{x}. \quad (4.11)$$

Proof. Define the kinetic energy \mathcal{E}_K^n , electric energy \mathcal{E}_E^n and magnetic energy \mathcal{E}_B^n at time t^n as

$$\mathcal{E}_K^n = \frac{1}{2} \int_{\Omega} \rho^n (|\mathbf{u}^n|^2 + 3\mathcal{T}^n) d\mathbf{x}, \quad \mathcal{E}_E^n = \frac{1}{2} \int_{\Omega} |\mathbf{E}^n|^2 d\mathbf{x}, \quad \mathcal{E}_B^n = \frac{1}{2} \int_{\Omega} |\mathbf{B}^n|^2 d\mathbf{x}. \quad (4.12)$$

It follows from (2.7) that the kinetic energy \mathcal{E}_K^n can also be written as

$$\mathcal{E}_K^n = \frac{1}{2} \int_{\Omega} \int_{\mathbb{R}^3} |\mathbf{v}|^2 f^n d\mathbf{v} d\mathbf{x}. \quad (4.13)$$

For the convection step, multiplying (4.6a) with $|\mathbf{v}|^2$ and integrating with respect to \mathbf{v} and \mathbf{x} over $\Omega \times \mathbb{R}^3$, yielding

$$\begin{aligned} \int_{\mathbb{R}^3} \int_{\Omega} \frac{f^{n+1,*} - f^n}{\Delta t} |\mathbf{v}|^2 d\mathbf{x} d\mathbf{v} &= - \int_{\mathbb{R}^3} \int_{\Omega} \mathbf{v} \cdot \nabla_{\mathbf{x}} f^n |\mathbf{v}|^2 d\mathbf{x} d\mathbf{v} \\ &= - \int_{\mathbb{R}^3} |\mathbf{v}|^2 \mathbf{v} \cdot \int_{\Omega} \nabla_{\mathbf{x}} f^n d\mathbf{x} d\mathbf{v} = 0, \end{aligned} \quad (4.14)$$

where the last equality is due to the periodic boundary conditions in \mathbf{x} . Therefore,

$$\mathcal{E}_K^{n+1,*} = \mathcal{E}_K^n. \quad (4.15)$$

For the Lorentz force step, the thermal energy is unchanged according to (4.8), i.e.,

$$\frac{3}{2} \int_{\Omega} \rho^{n+1} \mathcal{T}^{n+1} d\mathbf{x} = \frac{3}{2} \int_{\Omega} \rho^{n+1,*} \mathcal{T}^{n+1,*} d\mathbf{x}. \quad (4.16)$$

On the other hand, multiplying (4.6b) with $\mathbf{B}^{n+1} + \mathbf{B}^n$, (4.6c) with $\mathbf{E}^{n+1} + \mathbf{E}^n$, (4.6d) with $\rho^{n+1}(\mathbf{u}^{n+1} + \mathbf{u}^{n+1,*})$, and integrating with respect to \mathbf{x} over Ω , we obtain

$$\begin{aligned} \int_{\Omega} \frac{|\mathbf{B}^{n+1}|^2 - |\mathbf{B}^n|^2}{\Delta t} d\mathbf{x} &= - \int_{\Omega} \nabla_{\mathbf{x}} \times \frac{\mathbf{E}^{n+1} + \mathbf{E}^n}{2} \cdot (\mathbf{B}^{n+1} + \mathbf{B}^n) d\mathbf{x}, \\ \int_{\Omega} \frac{|\mathbf{E}^{n+1}|^2 - |\mathbf{E}^n|^2}{\Delta t} d\mathbf{x} &= \int_{\Omega} \nabla_{\mathbf{x}} \times \frac{\mathbf{B}^{n+1} + \mathbf{B}^n}{2} \cdot (\mathbf{E}^{n+1} + \mathbf{E}^n) d\mathbf{x} - \int_{\Omega} \mathbf{J}^{n+1/2} \cdot (\mathbf{E}^{n+1} + \mathbf{E}^n) d\mathbf{x}, \\ \int_{\Omega} \frac{\rho^{n+1}(|\mathbf{u}^{n+1}|^2 - |\mathbf{u}^{n+1,*}|^2)}{\Delta t} d\mathbf{x} &= \int_{\Omega} \rho^{n+1} \frac{\mathbf{E}^{n+1} + \mathbf{E}^n}{2} \cdot (\mathbf{u}^{n+1} + \mathbf{u}^{n+1,*}) d\mathbf{x} \\ &\quad + \int_{\Omega} \rho^{n+1} \frac{(\mathbf{u}^{n+1} + \mathbf{u}^{n+1,*})}{2} \times \frac{\mathbf{B}^{n+1} + \mathbf{B}^n}{2} \cdot (\mathbf{u}^{n+1} + \mathbf{u}^{n+1,*}) d\mathbf{x}. \end{aligned} \quad (4.17)$$

Summing up (4.16) and (4.17), together with (4.8) and (4.9), we have

$$\begin{aligned} &(\mathcal{E}_K^{n+1} + \mathcal{E}_E^{n+1} + \mathcal{E}_B^{n+1}) - (\mathcal{E}_K^{n+1,*} + \mathcal{E}_E^n + \mathcal{E}_B^n) \\ &= \frac{\Delta t}{2} \int_{\Omega} \nabla_{\mathbf{x}} \times (\mathbf{B}^{n+1} + \mathbf{B}^n) \cdot (\mathbf{E}^{n+1} + \mathbf{E}^n) - \nabla_{\mathbf{x}} \times (\mathbf{E}^{n+1} + \mathbf{E}^n) \cdot (\mathbf{B}^{n+1} + \mathbf{B}^n) d\mathbf{x} \\ &= \frac{\Delta t}{2} \int_{\Omega} \nabla_{\mathbf{x}} \cdot [(\mathbf{B}^{n+1} + \mathbf{B}^n) \times (\mathbf{E}^{n+1} + \mathbf{E}^n)] d\mathbf{x} = 0, \end{aligned} \quad (4.18)$$

where the last equality holds due to the periodic boundary conditions in \mathbf{x} . We complete the proof by combining (4.18) with (4.15), yielding

$$\mathcal{E}_{\text{total}}^{n+1} \triangleq (\mathcal{E}_K^{n+1} + \mathcal{E}_E^{n+1} + \mathcal{E}_B^{n+1}) = (\mathcal{E}_K^{n+1,*} + \mathcal{E}_E^n + \mathcal{E}_B^n) \triangleq \mathcal{E}_{\text{total}}^n. \quad (4.19)$$

□

From this theorem, we can see that **Scheme-I** exactly preserves the total energy. This scheme can potentially work for the VM system when stiffness occurs in the electromagnetic field, since (4.6b), (4.6c) and (4.6d) are formulated using the implicit midpoint method on $(\mathbf{E}, \mathbf{B}, \mathbf{u})$. However, the computation of this scheme is demanding and requires inversion of a nonlinear high-dimensional coupled system. To improve the efficiency and reduce computational cost, we modify **Scheme-I** by advancing the magnetic field explicitly, and denote the resulting scheme as **Scheme-II**, which is designed as follows

Scheme-II: Explicit for the magnetic field

$$\frac{f^{n+1,*} - f^n}{\Delta t} = -\mathbf{v} \cdot \nabla_{\mathbf{x}} f^n, \quad (4.20a)$$

$$\frac{\mathbf{B}^{n+1/2} - \mathbf{B}^n}{\Delta t/2} = -\nabla_{\mathbf{x}} \times \mathbf{E}^n, \quad (4.20b)$$

$$\frac{\mathbf{E}^{n+1} - \mathbf{E}^n}{\Delta t} = \nabla_{\mathbf{x}} \times \mathbf{B}^{n+1/2} - \mathbf{J}^{n+1/2}, \quad (4.20c)$$

$$\frac{\mathbf{B}^{n+1} - \mathbf{B}^{n+1/2}}{\Delta t/2} = -\nabla_{\mathbf{x}} \times \mathbf{E}^{n+1}, \quad (4.20d)$$

$$\frac{\mathbf{u}^{n+1} - \mathbf{u}^{n+1,*}}{\Delta t} = \frac{\mathbf{E}^n + \mathbf{E}^{n+1}}{2} + \frac{\mathbf{u}^{n+1,*} + \mathbf{u}^{n+1}}{2} \times \mathbf{B}^{n+1/2}, \quad (4.20e)$$

$$\frac{f_{\alpha}^{n+1} - f_{\alpha}^{n+1,*}}{\Delta t} = \sum_{d,l,m=1}^3 \epsilon_{dlm} (\alpha_l + 1) B_m^{n+1/2} f_{\alpha-e_d+e_l}^{n+1,*}, \quad 2 \leq |\alpha| \leq M, \quad (4.20f)$$

where $\mathbf{J}^{n+1/2}$ is defined the same as in (4.7). $\rho^{n+1,*}$, $\mathbf{u}^{n+1,*}$ are connected with $f^{n+1,*}$ in (4.20a) and (2.7). (4.8) and (4.9) also hold here.

Theorem 2 (Total energy conservation of **Scheme-II**). ***Scheme-II** preserves the discrete total energy $\mathcal{E}_{\text{total}}^n = \mathcal{E}_{\text{total}}^{n+1}$ of the VM system in Sec. 2 with periodic boundary conditions in \mathbf{x} , where*

$$\mathcal{E}_{\text{total}}^n = \frac{1}{2} \int_{\Omega} \rho^n (|\mathbf{u}^n|^2 + 3\mathcal{T}^n) d\mathbf{x} + \frac{1}{2} \int_{\Omega} |\mathbf{E}^n|^2 + \mathbf{B}^{n+1/2} \cdot \mathbf{B}^{n-1/2} d\mathbf{x}. \quad (4.21)$$

Proof. The change of the kinetic energy in the convection step and the thermal energy in the Lorentz force step are the same as (4.15) and (4.16) in Theorem 1. For the Lorentz force step, at time level $n+1$, (4.20b) becomes

$$\frac{\mathbf{B}^{n+3/2} - \mathbf{B}^{n+1}}{\Delta t/2} = -\nabla_{\mathbf{x}} \times \mathbf{E}^{n+1}, \quad (4.22)$$

which, combining with (4.20d), yields

$$\frac{\mathbf{B}^{n+3/2} - \mathbf{B}^{n+1/2}}{\Delta t} = -\nabla_{\mathbf{x}} \times \mathbf{E}^{n+1}, \quad \frac{\mathbf{B}^{n+1/2} - \mathbf{B}^{n-1/2}}{\Delta t} = -\nabla_{\mathbf{x}} \times \mathbf{E}^n. \quad (4.23)$$

Multiplying (4.23) with $\mathbf{B}^{n+1/2}$, (4.20c) with $\mathbf{E}^{n+1} + \mathbf{E}^n$, (4.20e) with $\rho^{n+1}(\mathbf{u}^{n+1} + \mathbf{u}^{n+1,*})$, and integrating with respect to \mathbf{x} over Ω , we obtain

$$\begin{aligned} \int_{\Omega} \frac{(\mathbf{B}^{n+3/2} - \mathbf{B}^{n+1/2}) \cdot \mathbf{B}^{n+1/2}}{\Delta t} d\mathbf{x} &= - \int_{\Omega} \nabla_{\mathbf{x}} \times \mathbf{E}^{n+1} \cdot \mathbf{B}^{n+1/2} d\mathbf{x}, \\ \int_{\Omega} \frac{(\mathbf{B}^{n+1/2} - \mathbf{B}^{n-1/2}) \cdot \mathbf{B}^{n+1/2}}{\Delta t} d\mathbf{x} &= - \int_{\Omega} \nabla_{\mathbf{x}} \times \mathbf{E}^n \cdot \mathbf{B}^{n+1/2} d\mathbf{x}, \\ \int_{\Omega} \frac{|\mathbf{E}^{n+1}|^2 - |\mathbf{E}^n|^2}{\Delta t} d\mathbf{x} &= \int_{\Omega} \nabla_{\mathbf{x}} \times \mathbf{B}^{n+1/2} \cdot (\mathbf{E}^{n+1} + \mathbf{E}^n) d\mathbf{x} - \int_{\Omega} \mathbf{J}^{n+1/2} \cdot (\mathbf{E}^{n+1} + \mathbf{E}^n) d\mathbf{x}, \\ \int_{\Omega} \frac{\rho^{n+1}(|\mathbf{u}^{n+1}|^2 - |\mathbf{u}^{n+1,*}|^2)}{\Delta t} d\mathbf{x} &= \int_{\Omega} \rho^{n+1} \frac{\mathbf{E}^{n+1} + \mathbf{E}^n}{2} \cdot (\mathbf{u}^{n+1} + \mathbf{u}^{n+1,*}) d\mathbf{x} \\ &\quad + \int_{\Omega} \rho^{n+1} \frac{(\mathbf{u}^{n+1} + \mathbf{u}^{n+1,*})}{2} \times \mathbf{B}^{n+1/2} \cdot (\mathbf{u}^{n+1} + \mathbf{u}^{n+1,*}) d\mathbf{x}. \end{aligned} \quad (4.24)$$

Define the magnetic energy \mathcal{E}_B^{n+1} as

$$\mathcal{E}_B^n = \frac{1}{2} \int_{\Omega} \mathbf{B}^{n+1/2} \cdot \mathbf{B}^{n-1/2} d\mathbf{x}. \quad (4.25)$$

Summing up (4.24) and (4.16), together with (4.8) and (4.9), we have

$$\begin{aligned} &(\mathcal{E}_K^{n+1} + \mathcal{E}_E^{n+1} + \mathcal{E}_B^{n+1}) - (\mathcal{E}_K^{n+1,*} + \mathcal{E}_E^n + \mathcal{E}_B^n) \\ &= \Delta t \int_{\Omega} \nabla_{\mathbf{x}} \times \mathbf{B}^{n+1/2} \cdot (\mathbf{E}^{n+1} + \mathbf{E}^n) - \nabla_{\mathbf{x}} \times (\mathbf{E}^{n+1} + \mathbf{E}^n) \cdot \mathbf{B}^{n+1/2} d\mathbf{x} \\ &= \Delta t \int_{\Omega} \nabla_{\mathbf{x}} \cdot [\mathbf{B}^{n+1/2} \cdot (\mathbf{E}^{n+1} + \mathbf{E}^n)] d\mathbf{x} = 0, \end{aligned} \quad (4.26)$$

where the last equality is due to periodic boundary conditions in \mathbf{x} . We complete the proof. \square

Similar as studied in [10], **Scheme-II** achieves near conservation of the total energy. The total energy (4.21) of **Scheme-II** is a modified second-order version of the exact total energy defined in (4.11). This ensures that over the long run, the numerical energy will not deviate much from its actual value. Total energy conservation is preserved with a suitable time step size in the numerical simulations.

It is worth mentioning that although **Scheme-II** is formulated by using the leap frog method for Maxwell's equations in (4.20b)-(4.20d), \mathbf{E}^{n+1} and \mathbf{u}^{n+1} are advanced implicitly via (4.6c) and (4.20e), since $\mathbf{J}^{n+1/2}$ defined in (4.7) involves the information of \mathbf{u}^{n+1} . Comparing with **Scheme-I**, **Scheme-II** deals with a smaller linear system, where the matrix form for updating \mathbf{u} and \mathbf{E} to the next time level is given by

$$\left(I + \frac{\Delta t}{2} \begin{bmatrix} 0 & \rho^{n+1} & \rho^{n+1} \\ -1 & 0 & -B_3^{n+1/2} \\ -1 & B_3^{n+1/2} & 0 \end{bmatrix} \right) \begin{bmatrix} E_1^{n+1} \\ E_2^{n+1} \\ E_3^{n+1} \\ u_1^{n+1} \\ u_2^{n+1} \\ u_3^{n+1} \end{bmatrix} = \text{RHS}^{n+1,*}. \quad (4.27)$$

Remark 1. By setting $\mathbf{B} = \mathbf{0}$ in **Scheme-I** and **Scheme-II**, both energy-preserving schemes can be extended to the VA system (2.6) in the framework of moment methods, given as follows

$$\frac{f^{n+1,*} - f^n}{\Delta t} = -\mathbf{v} \cdot \nabla_{\mathbf{x}} f^n, \quad (4.28a)$$

$$\frac{\mathbf{E}^{n+1} - \mathbf{E}^n}{\Delta t} = -\mathbf{J}^{n+1/2}, \quad (4.28b)$$

$$\frac{\mathbf{u}^{n+1} - \mathbf{u}^{n+1,*}}{\Delta t} = \frac{\mathbf{E}^n + \mathbf{E}^{n+1}}{2}. \quad (4.28c)$$

4.2 Fully discrete scheme and its properties

In this section, the fully discrete numerical scheme to solve the VM system is introduced. Compared with **Scheme-I**, **Scheme-II** is far more efficient, therefore, **Scheme-II** will be adopted in the following sections.

4.2.1 Fully discrete scheme

In this section, we describe the details of the spatial discretization coupling with the temporal discretization in **Scheme-II** to formulate the fully discrete scheme.

First, the spatial domain $\Omega \subset \mathbb{R}^3$ is taken a uniform partition into cubic meshes $\{T_{\mathbf{j}}\}$ with $\mathbf{j} = (j_1, j_2, j_3)$. Denote the mesh size as $\Delta \mathbf{x} = (\Delta x_1, \Delta x_2, \Delta x_3)$. Let $f_{\mathbf{j}}^n(\mathbf{v})$ denote the numerical approximation to $f(t, \mathbf{x}, \mathbf{v})$ in the mesh $T_{\mathbf{j}}$ at time t^n . The Hermite expansion for $f_{\mathbf{j}}^n(\mathbf{v})$ is

$$f_{\mathbf{j}}^n(t, \mathbf{v}) = \sum_{|\alpha| \leq M} f_{\alpha, \mathbf{j}}^n \mathcal{H}_{\mathcal{T}_{\mathbf{j}}^n, \alpha} \left(\frac{\mathbf{v} - \mathbf{u}_{\mathbf{j}}^n}{\sqrt{\mathcal{T}_{\mathbf{j}}^n}} \right). \quad (4.29)$$

We further denote $\mathbf{E}_{\mathbf{j}}^n$ and $\mathbf{B}_{\mathbf{j}}^n$ as the numerical approximations to the electric field \mathbf{E} and the magnetic field \mathbf{B} in the mesh $T_{\mathbf{j}}$ at time t^n , respectively.

For the convection step, we follow the numerical scheme in [5, 40] with the fully discrete scheme for $f_{\mathbf{j}}^n$ given by

$$\frac{f_{\mathbf{j}}^{n+1,*} - f_{\mathbf{j}}^n}{\Delta t} = - \sum_{d=1}^3 \frac{1}{\Delta x_d} \left(F_{\mathbf{j}+e_d/2}^n - F_{\mathbf{j}-e_d/2}^n \right) - \sum_{d=1}^3 \frac{1}{\Delta x_d} \left(R_{\mathbf{j}+e_d/2}^{n-} - R_{\mathbf{j}-e_d/2}^{n+} \right), \quad (4.30)$$

with $F_{\mathbf{j} \pm e_d/2}^n$ and $R_{\mathbf{j} \pm e_d/2}^{n \pm}$ being the numerical fluxes. For the non-conserved flux $R_{\mathbf{j}+e_d/2}^{n+}$, we adopt the same recipe in [40] and thus omit the details here. For the flux $F_{\mathbf{j} \pm e_d/2}^n$, we adopt the

HLL flux

$$F_{j+e_d/2}^n = \begin{cases} v_d f_{j+e_d/2}^{n,(L)}, & \lambda_{j+e_d/2}^L \geq 0, \\ \frac{\lambda_{j+e_d/2}^R v_d f_{j+e_d/2}^{n,(L)} - \lambda_{j+e_d/2}^L v_d f_{j+e_d/2}^{n,(R)} + \lambda_{j+e_d/2}^L \lambda_{j+e_d/2}^R (f_{j+e_d/2}^{n,(R)} - f_{j+e_d/2}^{n,(L)})}{\lambda_{j+e_d/2}^R - \lambda_{j+e_d/2}^L}, & \lambda_{j+e_d/2}^L < 0 < \lambda_{j+e_d/2}^R, \\ v_d f_{j+e_d/2}^{n,(R)}, & \lambda_{j+e_d/2}^R \leq 0, \end{cases} \quad (4.31)$$

where $f_{j+e_d/2}^{n,(L)}$ and $f_{j+e_d/2}^{n,(R)}$ are the linear reconstruction of f_j^n

$$f_{j+e_d/2}^{n,(L)} = f_j^n + \frac{\Delta x_d}{2} \frac{f_{j+e_d}^n - f_{j-e_d}^n}{2\Delta x_d}, \quad f_{j+e_d/2}^{n,(R)} = f_j^n - \frac{\Delta x_d}{2} \frac{f_{j+e_d}^n - f_{j-e_d}^n}{2\Delta x_d}. \quad (4.32)$$

Here $\lambda_{j+e_d/2}^L$, $\lambda_{j+e_d/2}^R$ are the minimum and maximum characteristic velocities of the moment system, given by

$$\begin{aligned} \lambda_{j+e_d/2}^L &= \min \left\{ u_{d,j} - C_{M+1} \sqrt{\mathcal{T}_j^n}, u_{d,j+e_d} - C_{M+1} \sqrt{\mathcal{T}_{j+e_d}^n} \right\}, \\ \lambda_{j+e_d/2}^R &= \max \left\{ u_{d,j} + C_{M+1} \sqrt{\mathcal{T}_j^n}, u_{d,j+e_d} + C_{M+1} \sqrt{\mathcal{T}_{j+e_d}^n} \right\}, \end{aligned} \quad (4.33)$$

where C_{M+1} is the largest root of the Hermite polynomial $H_{M+1}(x)$.

For the Lorentz force step and Maxwell's equations, we apply the central finite difference scheme to discretize the spatial variable in (4.20b)-(4.20f) of **Scheme-II**, yielding

$$\frac{B_j^{n+1/2} - B_j^n}{\Delta t/2} = -\Pi_x E_j^n, \quad (4.34a)$$

$$\frac{E_j^{n+1} - E_j^n}{\Delta t} = \Pi_x B_j^{n+1/2} - J_j^{n+1/2}, \quad (4.34b)$$

$$\frac{B_j^{n+1} - B_j^{n+1/2}}{\Delta t/2} = -\Pi_x E_j^{n+1}, \quad (4.34c)$$

$$\frac{u_j^{n+1} - u_j^{n+1,*}}{\Delta t} = \frac{E_j^n + E_j^{n+1}}{2} + \frac{u_j^{n+1,*} + u_j^{n+1}}{2} \times B_j^{n+1/2}, \quad (4.34d)$$

$$\frac{f_{\alpha,j}^{n+1} - f_{\alpha,j}^{n+1,*}}{\Delta t} = \sum_{d,l,m=1}^3 \epsilon_{dlm} (\alpha_l + 1) B_{m,j}^{n+1/2} f_{\alpha-e_d+e_l,j}^{n+1,*}, \quad 2 \leq |\alpha| \leq M, \quad (4.34e)$$

where $\Pi_x \cdot$ is the discretization of the curl operator $\nabla_x \times \cdot$, defined as

$$\Pi_x S_j = \begin{vmatrix} \vec{j}_1 & \vec{j}_2 & \vec{j}_3 \\ D_1 & D_2 & D_3 \\ S_{1,j} & S_{2,j} & S_{3,j} \end{vmatrix}, \quad D_d S_j = \frac{S_{j+e_d} - S_{j-e_d}}{2\Delta x_d}, \quad d = 1, 2, 3. \quad (4.35)$$

The time step Δt of the above fully discrete scheme should satisfy the following CFL condition

$$\text{CFL} = \frac{\Delta t^n}{\Delta x_d} \max \left\{ \left| \lambda_{j+e_d/2}^R \right|, \left| \lambda_{j+e_d/2}^L \right| \right\} < 1, \quad d = 1, 2, 3, \quad (4.36)$$

with $\lambda_{j+e_d/2}^L$, $\lambda_{j+e_d/2}^R$ given in (4.33).

4.2.2 Outline of the algorithm

The overall numerical scheme is summarized as follows:

1. Let $n = 0$ and set the initial value of $f_{\alpha,j}^0$, E_j^0 , and B_j^0 ;

2. Set Δt^n according to the CFL condition (4.36);
3. Update the convection term to obtain $f_j^{n+1,*}$ using (4.30);
4. Obtain $\rho_j^{n+1,*}$, $\mathcal{T}_j^{n+1,*}$ and $\mathbf{u}_j^{n+1,*}$ using (2.5) and (2.7);
5. Update \mathbf{u}_j^{n+1} , \mathbf{E}_j^{n+1} and \mathbf{B}_j^{n+1} and $f_{\alpha,j}^{n+1}$ using (4.34);
6. Reset the expansion center and scaling factor in the mesh T_j with \mathbf{u}_j^{n+1} and \mathcal{T}_j^{n+1} ;
7. Project f_j^{n+1} to the functional space with expansion center \mathbf{u}_j^{n+1} and \mathcal{T}_j^{n+1} ;
8. Let $n \leftarrow n + 1$, and return to Step 2.

In the framework of the regularized moment method, it is restricted that the expansion center should be the local macroscopic velocity and the scaling factor should be the local temperature. Therefore, in Step 7 of the algorithm, the distribution function is projected into the corresponding space. The total computational cost of this projection is $\mathcal{O}(M^3)$, see e.g. [5] for more details.

4.2.3 Conservation properties of the fully discrete scheme

In this subsection, we present conservation properties of the fully discrete scheme and defer a rigorous proof of these properties.

Denote the discrete mass and total energy of the fully discrete scheme as

$$\mathcal{P}_h^n = \sum_{j \in \mathbf{J}} \Delta V \rho_j^n, \quad \mathcal{E}_{\text{total},h}^n = \frac{\Delta V}{2} \sum_{j \in \mathbf{J}} \left[\rho_j^n (\mathbf{u}_j^n)^2 + 3\rho_j^n \mathcal{T}_j^n + (\mathbf{E}_j^n)^2 + \mathbf{B}_j^{n-1/2} \mathbf{B}_j^{n+1/2} \right], \quad (4.37)$$

where $\Delta V = \prod_{d=1}^3 \Delta x_d$ is the mesh volume and \mathbf{J} is the total set of mesh indexes. We establish conservation properties of the fully discrete scheme in the following theorem.

Theorem 3. *The fully discrete scheme preserves the discrete mass and total energy*

$$\mathcal{P}_h^{n+1} = \mathcal{P}_h^n, \quad \mathcal{E}_{\text{total},h}^{n+1} = \mathcal{E}_{\text{total},h}^n, \quad (4.38)$$

for the VM system with periodic boundary conditions in \mathbf{x} .

Proof. The proof of the mass conservation is similar to [5], and is thus omitted.

The total energy conservation will be proved in two steps as in the proof of Theorem 2 in Sec. 4.1. For the convection step, by multiplying (4.30) with $|\mathbf{v}|^2$ and integrating with respect to \mathbf{v} , it holds

$$\int_{\mathbb{R}^3} |\mathbf{v}|^2 \frac{f_j^{n+1,*} - f_j^n}{\Delta t} d\mathbf{v} = \int_{\mathbb{R}^3} |\mathbf{v}|^2 \left(- \sum_{d=1}^3 \frac{1}{\Delta x_d} \left(F_{j+e_d/2}^n - F_{j-e_d/2}^n \right) - \sum_{d=1}^3 \frac{1}{\Delta x_d} \left(R_{j+e_d/2}^{n-} - R_{j-e_d/2}^{n+} \right) \right) d\mathbf{v}. \quad (4.39)$$

Summing (4.39) for all $j \in \mathbf{J}$, together with periodic boundary conditions in \mathbf{x} and the fact that the regularization term only revises the moment coefficients at the highest order and does not change the total energy, we have

$$\mathcal{E}_{K,h}^{n+1,*} \triangleq \frac{\Delta V}{2} \sum_{j \in \mathbf{J}} \int_{\mathbb{R}^3} |\mathbf{v}|^2 f_j^{n+1,*} d\mathbf{v} = \frac{\Delta V}{2} \sum_{j \in \mathbf{J}} \int_{\mathbb{R}^3} |\mathbf{v}|^2 f_j^n d\mathbf{v} \triangleq \mathcal{E}_{K,h}^n. \quad (4.40)$$

For the Lorentz force step, (4.34a) at time level $n + 1$ is

$$\frac{\mathbf{B}_j^{n+3/2} - \mathbf{B}_j^{n+1}}{\Delta t/2} = -\Pi_{\mathbf{x}} \mathbf{E}_j^{n+1}. \quad (4.41)$$

which, combining with (4.34c), yields

$$\frac{B_j^{n+3/2} - B_j^{n+1/2}}{\Delta t} = -\Pi_x \mathbf{E}_j^{n+1}, \quad \frac{B_j^{n+1/2} - B_j^{n-1/2}}{\Delta t} = -\Pi_x \mathbf{E}_j^n. \quad (4.42)$$

Similarly as in the proof of Theorem 2, summing up (4.42) for j , we obtain

$$\begin{aligned} & (\mathcal{E}_{K,h}^{n+1} + \mathcal{E}_{E,h}^{n+1} + \mathcal{E}_{B,h}^{n+1}) - (\mathcal{E}_{K,h}^{n+1,*} + \mathcal{E}_{E,h}^n + \mathcal{E}_{B,h}^n) \\ &= \Delta t \Delta V \sum_{j \in J} \left[\Pi_x B_j^{n+1/2} \cdot (\mathbf{E}_j^{n+1} + \mathbf{E}_j^n) - \Pi_x (\mathbf{E}_j^{n+1} + \mathbf{E}_j^n) \cdot B_j^{n+1/2} \right], \\ &= \Delta t \Delta V \sum_{j \in J} \Pi_x \cdot \left(B_j^{n+1/2} \cdot (\mathbf{E}_j^{n+1} + \mathbf{E}_j^n) \right) = 0, \end{aligned} \quad (4.43)$$

with

$$\mathcal{E}_{E,h}^n = \frac{\Delta V}{2} \sum_{j \in J} |\mathbf{E}_j^n|^2, \quad \mathcal{E}_{B,h}^n = \frac{\Delta V}{2} \sum_{j \in J} B_j^{n+1/2} \cdot B_j^{n-1/2}, \quad (4.44)$$

where in the last equality of (4.43) we use the definition (4.35) and the periodic boundary conditions in \mathbf{x} . Then the proof is completed by collecting (4.40) and (4.43). \square

5 Numerical experiments

In this section, several experiments will be studied to verify this energy-preserving moment method. Precisely, three 1D2V and one 2D3V problems are tested. All the tests are computed on the model named Intel(R) Xeon(R) Gold 5218 CPU @ 2.30GHz with the technique of multi-thread adopted. We will begin from a simplified VM model, which is introduced in [12], where the distribution function only depends on $(x, v_1, v_2) \in \Omega \times \mathbb{R}^2$, $B_1 = B_2 = E_3 = 0$, and $f, \mathbf{B}, \mathbf{E}$ are periodic in the x -direction. Thus, the VM system (2.1) and (2.2) is reduced into

$$\frac{\partial f}{\partial t} + v_1 \frac{\partial f}{\partial x} + (E_1 + v_2 B_3) \frac{\partial f}{\partial v_1} + (E_2 - v_1 B_3) \frac{\partial f}{\partial v_2} = 0, \quad (5.1)$$

$$\frac{\partial B_3}{\partial t} = -\frac{\partial E_2}{\partial x}, \quad \frac{\partial E_1}{\partial t} = -\int_{\mathbb{R}^2} v_1 f(t, x, \mathbf{v}) d\mathbf{v}, \quad \frac{\partial E_2}{\partial t} = -\frac{\partial B_3}{\partial x} - \int_{\mathbb{R}^2} v_2 f(t, x, \mathbf{v}) d\mathbf{v}. \quad (5.2)$$

For this simplified model, the discretized electric energy, magnetic energy, and kinetic energy are reduced into

$$\mathcal{E}_{E,h}^n = \frac{\Delta x}{2} \sum_{j=1}^N [(E_{1,j}^n)^2 + (E_{2,j}^n)^2], \quad \mathcal{E}_{B,h}^n = \frac{\Delta x}{2} \sum_{j=1}^N B_{3,j}^{n+1/2} B_{3,j}^{n-1/2}, \quad (5.3)$$

$$\mathcal{E}_{K,h}^n = \frac{\Delta x}{2} \sum_{j=1}^N [\rho_j^n (u_{1,j}^n)^2 + \rho_j^n (u_{2,j}^n)^2 + 2\rho_j^n \mathcal{T}_j^n], \quad (5.4)$$

with N the total cell number and Δx the mesh size in the spatial space.

5.1 Linear Landau damping problem

We will begin from the linear Landau damping problem in the 1D2V case for the VA system (2.6). Landau damping refers to the phenomenon that the amplitude of a wave decreases due to the interaction between the particles and the wave, which was put forward in [23] and later has been verified by experiments [26]. The initial condition is set as

$$f(0, x, \mathbf{v}) = \frac{1}{2\pi} e^{-\frac{|\mathbf{v}-\mathbf{u}|^2}{2\mathcal{T}}} (1 + A \cos(kx)), \quad (x, \mathbf{v}) \in [0, L] \times \mathbb{R}^2, \quad (5.5)$$

with

$$\mathbf{u} = \mathbf{0}, \quad \mathcal{T} = 1, \quad L = \frac{2\pi}{k}. \quad (5.6)$$

Similar tests are also studied in [5, 30]. Here, A is the perturbation amplitude, and k is the wave number.

In Landau damping theory, a large number of slow particles absorb energy from the wave while relatively fewer particles transfer energy to the wave, resulting in particles and the wave tending to synchronize [14]. Thus, in this test, we pay attention to the time evolution of the electric field energy \mathcal{E}_E which is expected to decay exponentially almost with a fixed rate γ_L related to the wave number k [5].

In the simulation, the mesh number in the spatial space is set as $N_x = 500$ with linear reconstruction utilized. The moment number is chosen as $M = 30$. Two cases where $k = 0.3$, $A = 10^{-5}$ and $k = 0.4$, $A = 0.01$ are tested. The time evolution of the total electric energy $\mathcal{E}_{E,h}^n$ is shown in Fig. 1. We capture their local peak values of different curves, and obtain the damping slope $\gamma_{L,h}$ using the least-square approximation as in [5]. Fig. 1 shows that the numerical damping slope is consistent with the theoretical result [12]. The qualitative solution of the damping slope is presented in Tab. 1, where the error between the theoretical value γ_L and the numerical solution $\gamma_{L,h}$ is quite small with the corresponding wave number k .

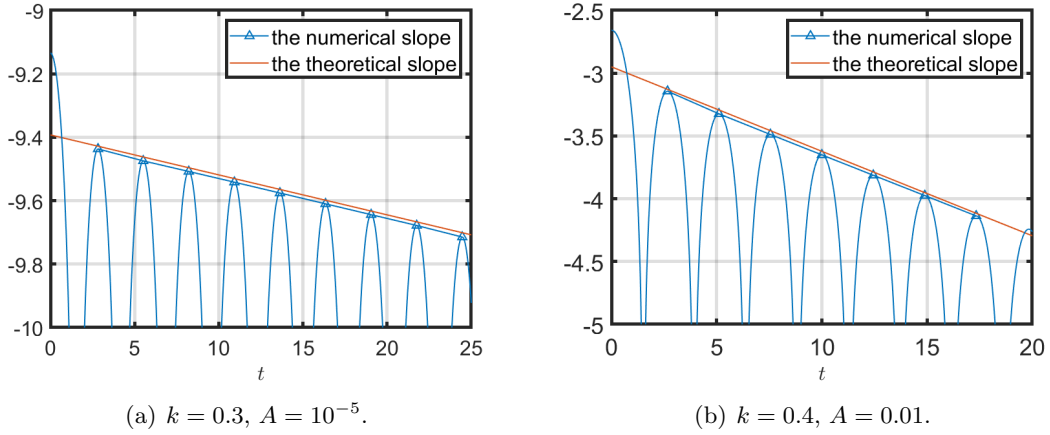


Figure 1: (Sec. 5.1) Time evolution of the total electric energy. Here, the x -axis is time t , and the y -axis is $[\log(2\mathcal{E}_{E,h}^n)]/2$ with $\mathcal{E}_{E,h}^n$ defined in (5.3).

Wave number k	Theoretic slope γ_L	Numerical slope $\gamma_{L,h}$
0.3	-0.0126	-0.0127
0.4	-0.0661	-0.0673

Table 1: (Sec. 5.1) The comparison of the theoretical and numerical slopes with different wave number k .

Landau damping only considers the self-consistent electric field of the particles, so the magnetic field energy is constant as zero. In this case, the total energy of the system is reduced into

$$\mathcal{E}_{\text{total},h}^n = \mathcal{E}_{K,h}^n + \mathcal{E}_{E,h}^n. \quad (5.7)$$

We define the variation of the total energy as

$$V(\mathcal{E}_{\text{total},h}^n) = |\mathcal{E}_{\text{total},h}^n - \mathcal{E}_{\text{total},h}^0|/|\mathcal{E}_{\text{total},h}^0|. \quad (5.8)$$

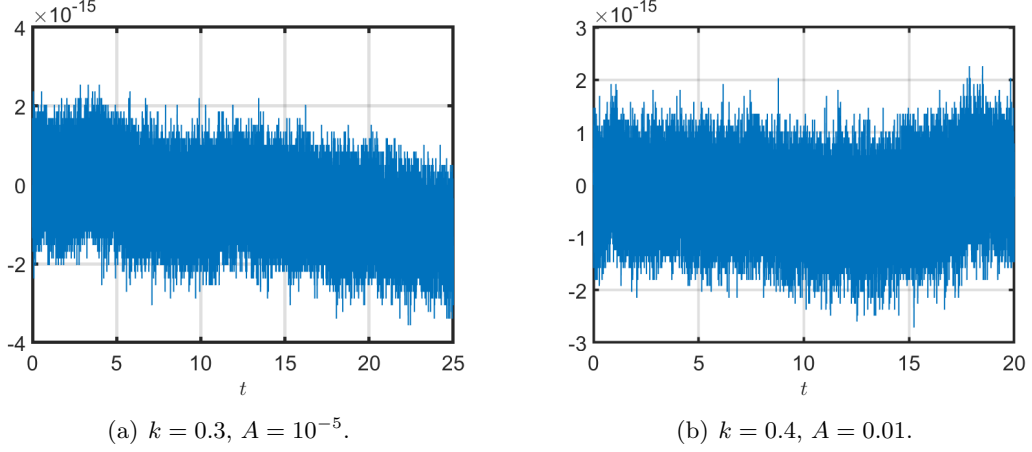


Figure 2: (Sec. 5.1) Time evolution of the relative error in total energy for the Landau damping test. Here, the x -axis is time t , and the y -axis is the relative error $V(\mathcal{E}_{\text{total},h}^n)$ defined in (5.8).

Fig. 2 shows the time evolution of the relative error $V(\mathcal{E}_{\text{total},h}^n)$. It illustrates that the error is quite small, almost reaching the machine error, which verifies the energy-preserving property of the numerical scheme.

5.2 Two-stream instability

In plasma physics, two-stream instability is a widespread and simple electrostatic micro-instability phenomenon [36]. When the charged particle beam passes through the plasma, the movement of the particles in the beam is disturbed, causing the particles to cluster, thus generating an electric field of space charges. This electric field encourages clustering, and leads to the dual-current instability. We choose the same initial condition as in [12]

$$f(0, x, \mathbf{v}) = \frac{\rho}{2\pi\mathcal{T}} \left[\frac{1}{2} \exp\left(-\frac{|\mathbf{v} - \mathbf{u}|^2}{2\mathcal{T}}\right) + \frac{1}{2} \exp\left(-\frac{|\mathbf{v} + \mathbf{u}|^2}{2\mathcal{T}}\right) \right], \quad (x, \mathbf{v}) \in [0, L] \times \mathbb{R}^2, \quad (5.9)$$

with

$$\rho = 1, \quad \mathbf{u} = (0.2, 0), \quad \mathcal{T} = 10^{-3}, \quad L = 2\pi. \quad (5.10)$$

Since that the magnetic effect will affect the magnetized plasma, we add the initial magnetic field perturbation instead of the general particle density perturbation to drive instability. Thus, the initial electric field and magnetic field are set as

$$\mathbf{E} = \mathbf{0}, \quad B_3(0, x) = A \sin(kx), \quad A = 10^{-3}, \quad k = 1. \quad (5.11)$$

In the simulation, the mesh number is set as $N = 200$, with linear reconstruction utilized in the spatial space, and the moment number is set as $M = 30$. Fig. 3(a) shows the time evolution for the electric, magnetic and kinetic energy defined in (5.3), where the numerical solution matches well with the reference solution by DVM. Fig. 3(b) shows the numerical solutions with the spatial size $N = 200, 400, 800$ and 1000 . It shows that the numerical solution by $N = 200$ is almost the same as that by $N = 1000$, which means that it has reached the converged solution, and even with $N = 200$, we can describe the behavior of the solution well. The marginal distribution

$$g(t, x, v_1) = \int_{\mathbb{R}} f(t, x, \mathbf{v}) dv_2 \quad (5.12)$$

is plotted in Fig. 4 to show the change in the distribution function. For the initial distribution, there exist two peaks, and the oscillations are appearing gradually, which we can clearly see

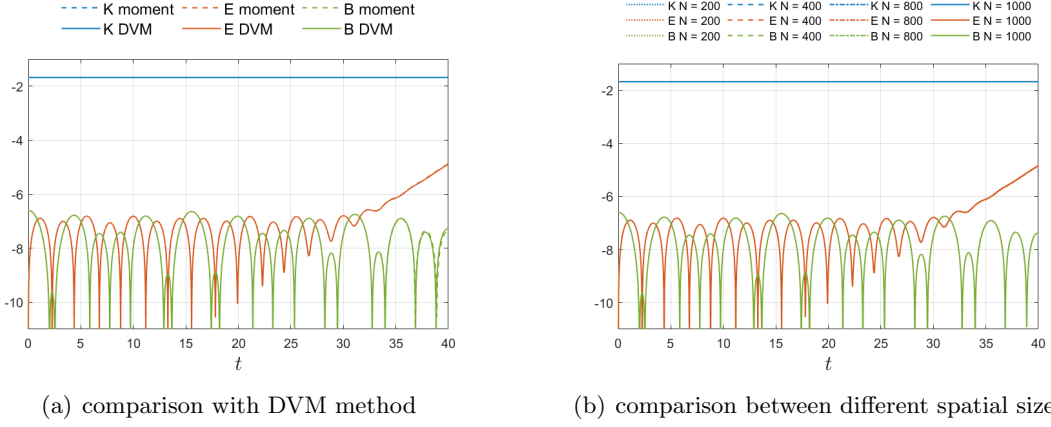


Figure 3: (Sec. 5.2) Time evolution of the kinetic energy $\mathcal{E}_{K,h}^n$, electric energy $\mathcal{E}_{E,h}^n$, and the magnetic energy $\mathcal{E}_{B,h}^n$. (a) The comparison with the reference solution by DVM. The dashed line is the numerical solution, and the bold line is the reference solution by DVM. (b) The comparison with different spatial sizes. Here, the spatial size is $N = 200, 400, 800$, and 1000 , respectively. In both figures, the x -axis is time, and the y -axis is the logarithmic form of the corresponding energy $\log_{10}(\mathcal{S}/L)$, $\mathcal{S} = \mathcal{E}_{K,h}^n, \mathcal{E}_{E,h}^n, \mathcal{E}_{B,h}^n$.

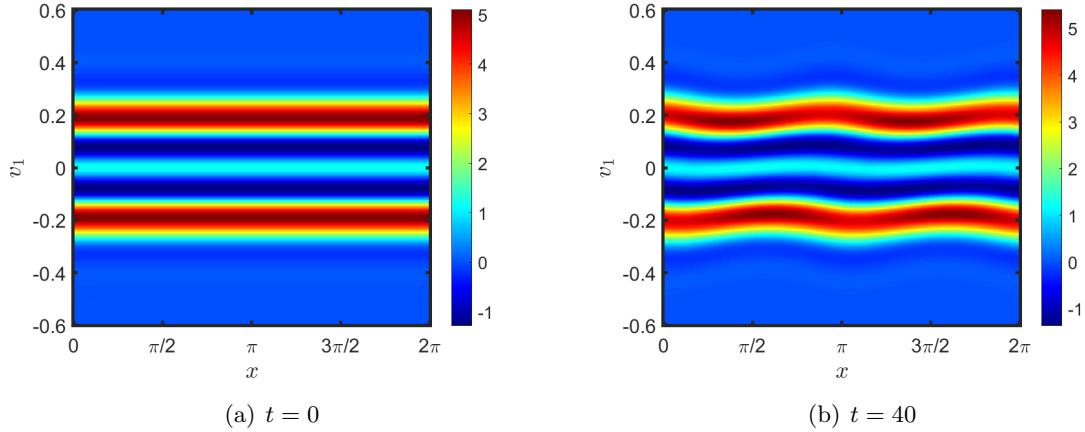


Figure 4: (Sec. 5.2) The marginal distribution function $g(t, x, v_1)$ at $t = 0$ and 40 .

at $t = 40$. The time evolution of the electric and magnetic field is shown in Fig. 5, where E_1 is quite small at the beginning, and then increases to some periodic structures from $t = 30$. For E_2 , it has the cos-type structure and then gradually changes with the periodic structure preserved. B_3 has the sin-type structure at the beginning, and is evolving with this structure kept. The electromagnetic behavior is also consistent with the setting of the initial condition. The reference solution by DVM is also illustrated in Fig. 5, where the two solutions are almost the same.

The time evolution of the relative error in total mass $V(\mathcal{P}_h^n)$ as

$$V(\mathcal{P}_h^n) = |\mathcal{P}_h^n - \mathcal{P}_h^0|/\mathcal{P}_h^0, \quad (5.13)$$

and that in total energy $V(\mathcal{E}_{\text{total},h}^n)$ is shown in Fig. 6(a) and 6(b). It illustrates that the total variation almost reaches the machine precision, which validates the excellent conservation of this numerical scheme. The variation of the electromagnetic energy and the kinetic energy is plotted in Fig. 6(c). Though, it seems constant in Fig. 3(a), the kinetic energy is changing at

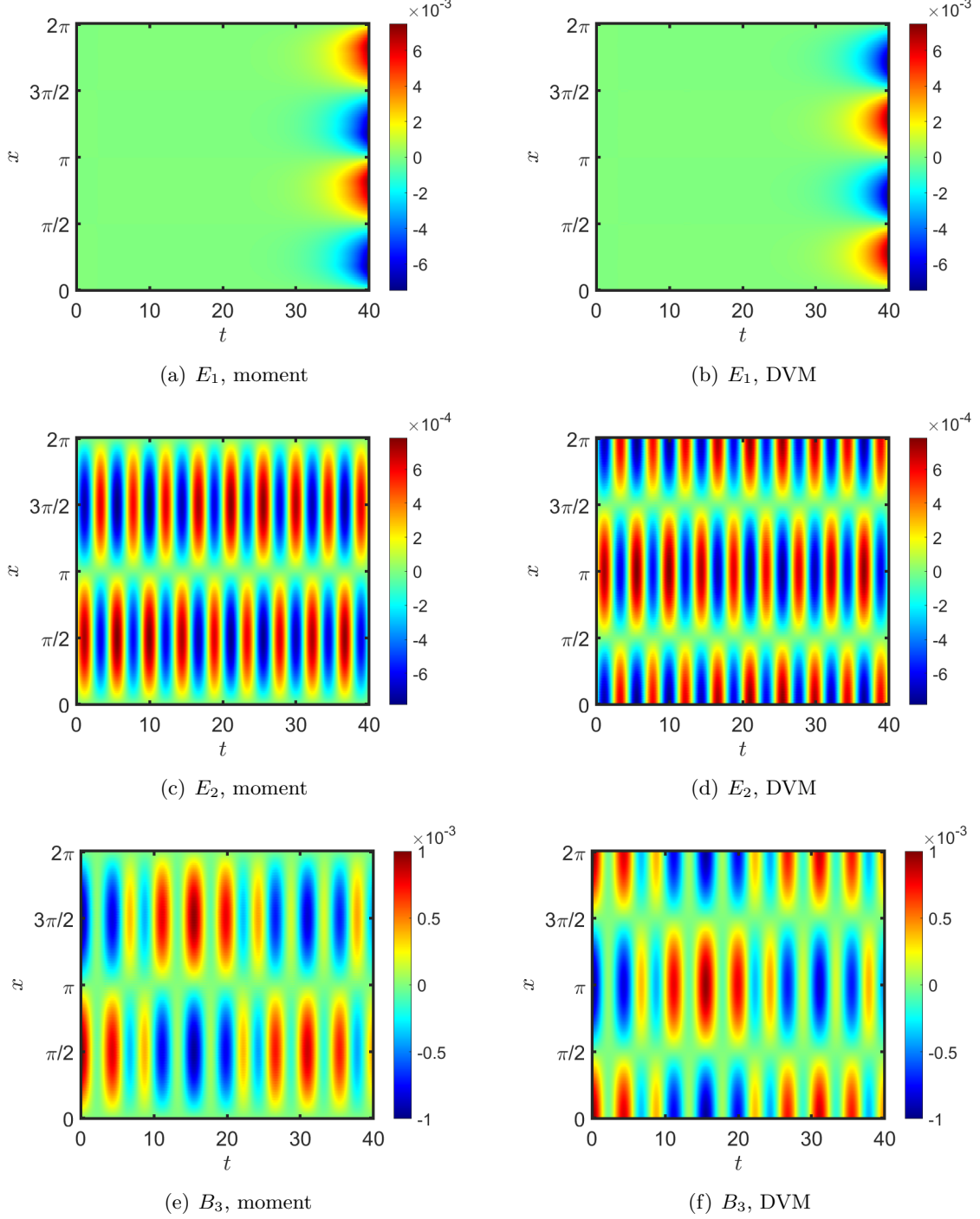


Figure 5: (Sec. 5.2) Time evolution of electric field E_1 , electric field E_2 , and magnetic field B_3 . The left column is the numerical solution by moment method, and the right column is the reference solution by DVM. Here, the x -axis is time t , and y -axis is the spatial space x .

the magnitude of $\mathcal{O}(10^{-5})$. Moreover, the variation of the kinetic and electromagnetic energy is almost the opposite, which also verifies the energy-preserving property of this numerical scheme.

5.3 Weibel instability

In this section, the Weibel instability will be studied. In the plasma, when the originally uniformly distributed electron current sheet is disturbed by the magnetic field, it will produce

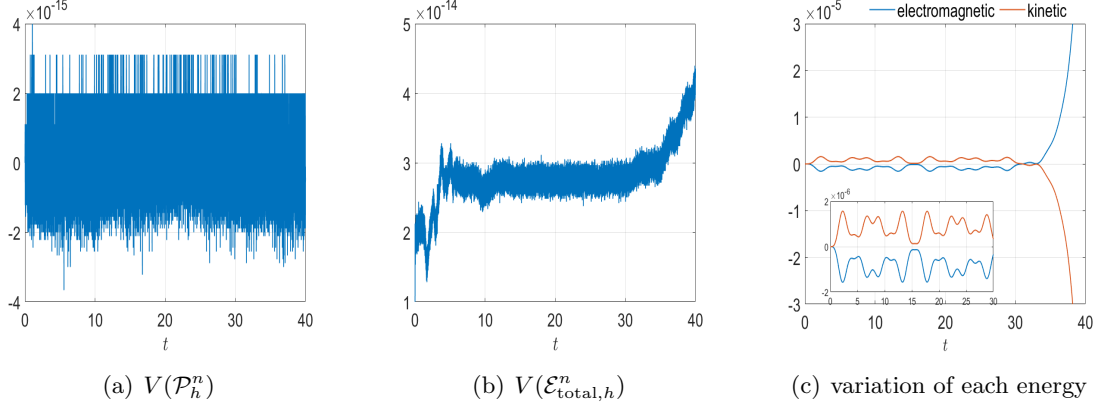


Figure 6: (Sec. 5.2) (a) Time evolution of the relative error in total mass $V(\mathcal{P}_h^n)$. (b) Time evolution of the relative error in total energy $V(\mathcal{E}_{\text{total},h}^n)$. (c) The variation of the electromagnetic $(\mathcal{E}_{B,h}^n + \mathcal{E}_{E,h}^n) - (\mathcal{E}_{B,h}^0 + \mathcal{E}_{E,h}^0)$ and the kinetic energy $(\mathcal{E}_{K,h}^n - \mathcal{E}_{K,h}^0)$. Here, the x -axis is time, and y -axis is the corresponding error.

a disturbance velocity. Then, the positive and negative current sheets are partly concentrated, and partly scattered, and will generate a disturbance current [2]. According to Faraday's law, the current disturbance in turn generates a new magnetic field. The increased local current density will also cause the plasma to be strongly pinched to form high-density filaments [2]. This is the so-called Weibel instability, which is also very common in plasma physics, especially astrophysics. As is in [10], the following initial non-symmetric condition is studied

$$f(0, x, \mathbf{v}) = \frac{\rho}{2\pi\mathcal{T}} \left[\frac{1}{6} \exp\left(-\frac{|\mathbf{v} - \mathbf{u}_1|^2}{2\mathcal{T}}\right) + \frac{5}{6} \exp\left(-\frac{|\mathbf{v} - \mathbf{u}_2|^2}{2\mathcal{T}}\right) \right], \quad (x, \mathbf{v}) \in [0, L] \times \mathbb{R}^2, \quad (5.14)$$

with

$$\rho(0, x) = 1, \quad \mathbf{u}_1 = (0, 0.5), \quad \mathbf{u}_2 = (0, -0.1), \quad \mathcal{T}(0, x) = 5 \cdot 10^{-3}. \quad (5.15)$$

The initial electric field is set as $\mathbf{E} = 0$, and the disturbance is given by the initial magnetic field as

$$B_3(0, x) = A \sin(kx), \quad A = 10^{-3}, \quad k = 0.2, \quad L = 2\pi/k = 10\pi. \quad (5.16)$$

In the simulation, the mesh number is set as $N = 2000$ with linear reconstruction utilized and the number of moments $M = 30$. Fig. 7 shows the time evolution of kinetic, magnetic, and electric energy. The electric energy in each spatial direction is also plotted. From Fig. 7, we can find that after the fast transient, the magnetic and electric energy are all increasing with oscillation, and the electric energy in the x -direction is quite small compared with that in the y -direction, which is unanimous with the setting of the initial condition. In Fig. 7(a), the reference solution by DVM is also plotted and the numerical solution is consistent with the reference solution. In Fig. 7(b), the numerical solutions of $\mathcal{E}_{K,h}^n, \mathcal{E}_{E,h}^h, \mathcal{E}_{B,h}^n$ and $\mathcal{E}_{E_1,h}^n$ with spatial sizes $N = 400, 800, 1000$ and 2000 are shown. Since $\mathcal{E}_{E_2,h}^n$ almost equals $\mathcal{E}_{E,h}^h$, we will omit it in Fig. 7(b). For different spatial sizes, the numerical solutions are on top of each other, which means that with $N = 400$, the numerical solution could describe the evolution of each energy well. The marginal distribution function $g(t, x, v_2)$ at $t = 0, 30, 50$ and 70 is illustrated in Fig. 8. At the initial moment, there are a high peak and a low peak, and the oscillations appear gradually. At $t = 70$, there exists an obvious sink in the middle of the distribution function. The time evolution of the electromagnetic field compared to the reference solution by DVM is shown in Fig. 9, where the magnitude of E_1 is the smallest, which is also consistent with the

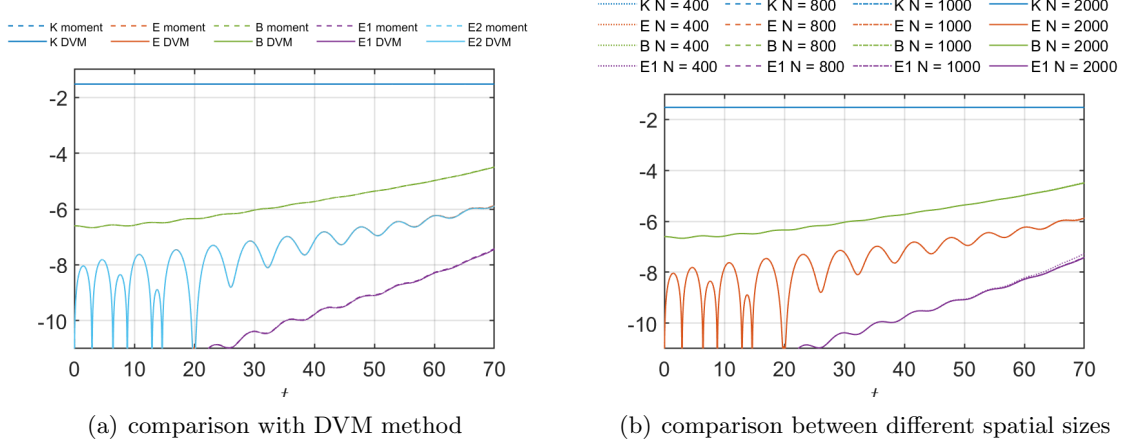


Figure 7: (Sec. 5.3) Time evolution of the kinetic energy $\mathcal{E}_{K,h}^n$, electric energy $\mathcal{E}_{E,h}^n$, the magnetic energy $\mathcal{E}_{B,h}^n$ and $\mathcal{E}_{E_i,h}^n$, $i = 1, 2$. (a) Comparison with the reference solution by DVM. The dashed line is the numerical solution, and the bold line is the reference solution by DVM. (b) Comparison with different spatial sizes. Here, the spatial size is $N = 400, 800, 1000$, and 2000 , respectively. In both figures, the x -axis is time, and the y -axis is the logarithmic form of the corresponding energy $\log_{10}(\mathcal{S}/L)$, $\mathcal{S} = \mathcal{E}_{K,h}^n, \mathcal{E}_{E,h}^n, \mathcal{E}_{B,h}^n, \mathcal{E}_{E_i,h}^n$, $i = 1, 2$.

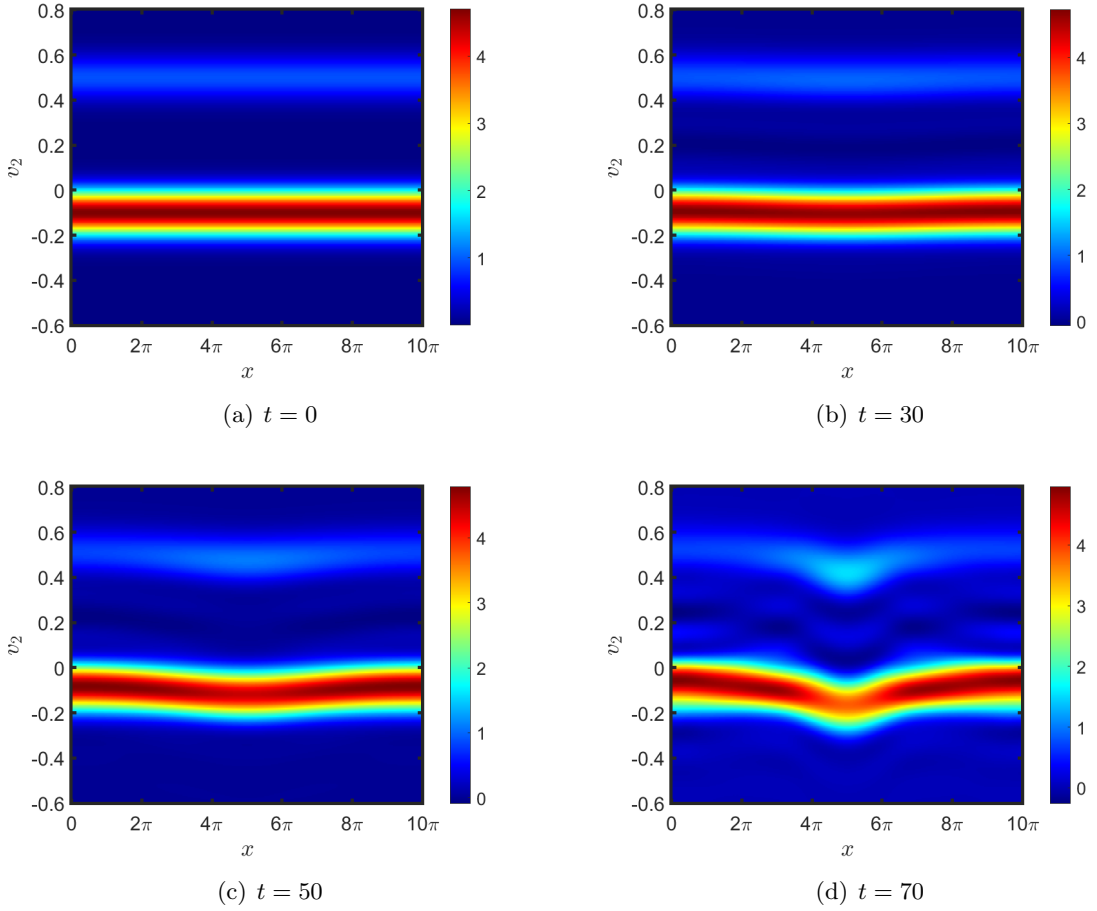


Figure 8: (Sec. 5.3) The marginal distribution function $g(t, x, v_2)$ at $t = 0, 30, 50$ and 70 .

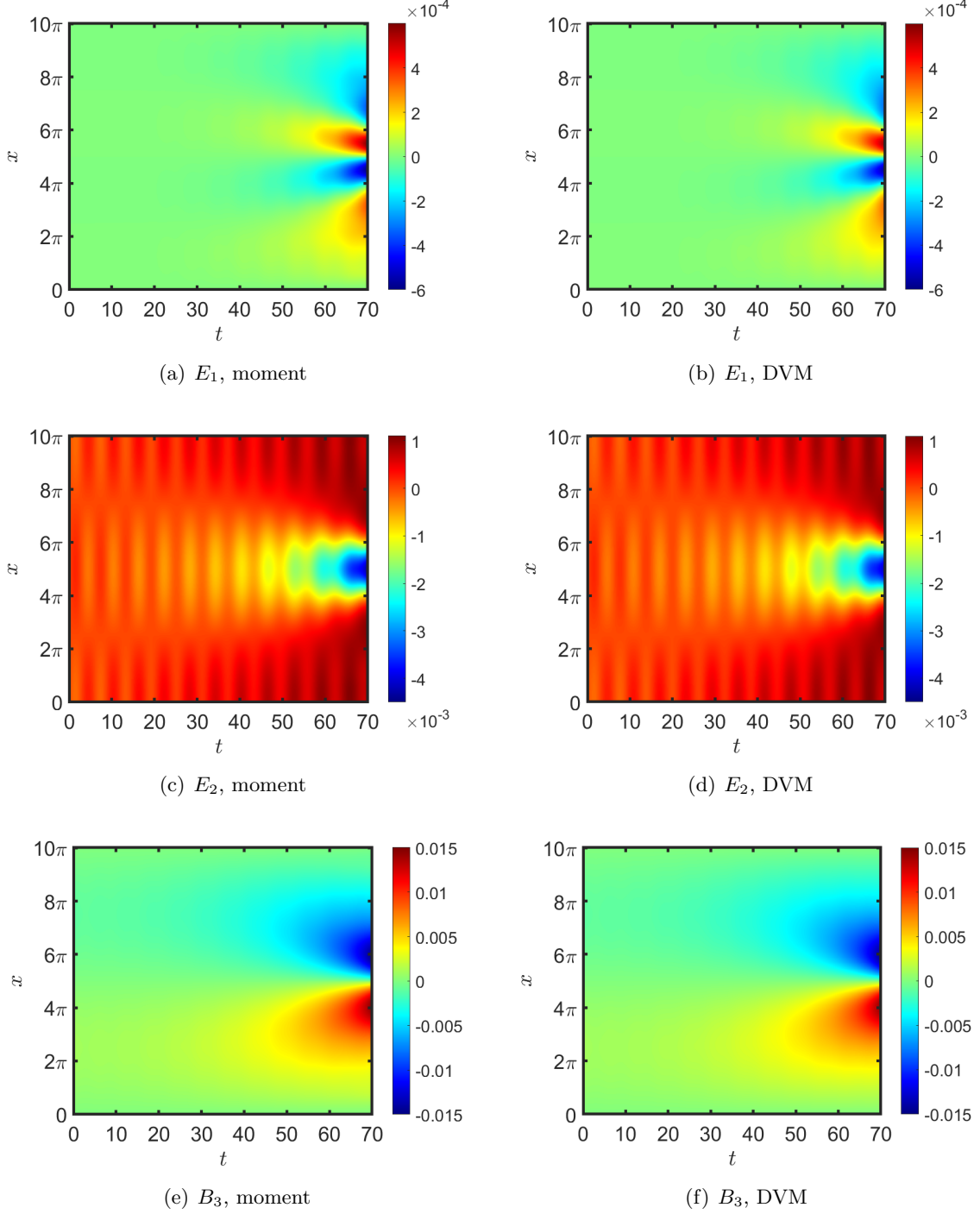


Figure 9: (Sec. 5.3) Time evolution of electric field E_1 , electric field E_2 , and magnetic field B_3 . The left column is the numerical solution by moment method, and the right column is the reference solution by DVM. Here, the x -axis is time t , and y -axis is the spatial space x .

numerical result in Fig. 7. Besides, the oscillations in E_2 , the periodic structure in E_1 and B_3 could be clearly seen.

The time evolution of the relative error in total mass and total energy is shown in Fig. 10. For the Weibel instability, the total variation of the mass and energy is still quite small, which validates the energy-preserving ability of this numerical scheme. The variation in electromagnetic and kinetic energy is plotted in Fig. 10(c), the behavior of which is similar to that of the two-stream instability, and we will not discuss more.

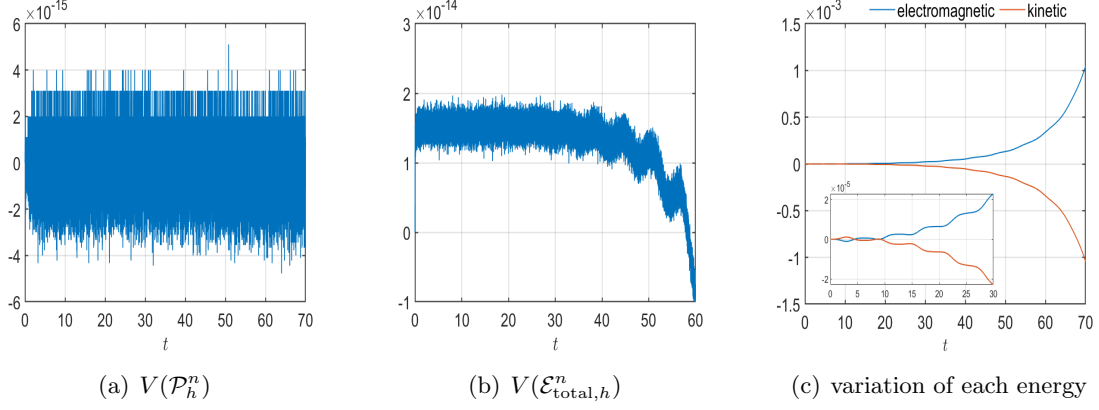


Figure 10: (Sec. 5.3) (a) Time evolution of the relative error in total mass $V(\mathcal{P}_h^n)$. (b) Time evolution of the relative error in total energy $V(\mathcal{E}_{\text{total},h}^n)$. (c) The variation of the electromagnetic $(\mathcal{E}_{B,h}^n + \mathcal{E}_{E,h}^n) - (\mathcal{E}_{B,h}^0 + \mathcal{E}_{E,h}^0)$ and kinetic energy $(\mathcal{E}_{K,h}^n - \mathcal{E}_{K,h}^0)$. Here, the x -axis is time, and y -axis is the corresponding error.

5.4 Orszag-Tang vortex

The Orszag-Tang vortex problem is a classic example of magnetohydrodynamics (MHD) [32]. It is an example of the interaction between large-scale fluid behavior and small-scale dissipation processes involving dynamic physics, which still interests a lot of research nowadays. The Orszag-Tang vortex problem describes the time evolution of ions and fluid electrons, and its initial condition will rapidly lead to broadband turbulence. In this section, we will try to study this problem using the energy-preserving moment method. The Orszag-Tang vortex problem is described by the multi-particle VM model, and we will introduce this model first.

A multi-particle model In a collisionless magnetized plasma, the normalized time evolution equation of the VM model with s species has the form below. The governing equation for the k -th species is

$$\frac{\partial f^k}{\partial t} + \nabla_{\mathbf{x}} \cdot (\mathbf{v} f^k) + \frac{q^k}{m^k} \frac{\omega_{ce}}{\omega_{pe}} (\mathbf{E} + \mathbf{v} \times \mathbf{B}) \cdot \nabla_{\mathbf{v}} f^k = 0, \quad k = 1, 2, \dots, s. \quad (5.17)$$

Similarly, the normalized Maxwell's equations describing the electromagnetic field have the form

$$\begin{cases} \frac{\partial \mathbf{E}}{\partial t} - \nabla_{\mathbf{x}} \times \mathbf{B} = -\frac{\omega_{pe}}{\omega_{ce}} \mathbf{J}, \\ \frac{\partial \mathbf{B}}{\partial t} + \nabla_{\mathbf{x}} \times \mathbf{E} = 0, \end{cases} \quad (5.18)$$

with Gauss's law as

$$\nabla_{\mathbf{x}} \cdot \mathbf{E} = \frac{\omega_{pe}}{\omega_{ce}} \rho_{\text{free}}, \quad \nabla_{\mathbf{x}} \cdot \mathbf{B} = 0. \quad (5.19)$$

Here, q^k and m^k are the normalized charge and mass of the k th species of particles. ω_{ce} and ω_{pe} are the electron cyclotron frequency and the electron plasma frequency. In the numerical simulation, we will pay attention to the ratio ω_{ce}/ω_{pe} instead of their specific value. Moreover, the electric density and current for the multi-particle VM model are defined as

$$\rho(t, \mathbf{x}) = \sum_{k=1}^s \rho^k = \sum_{k=1}^s q^k \int_{\mathbb{R}^3} f^k(t, \mathbf{x}, \mathbf{v}) d\mathbf{v}, \quad \mathbf{J}(t, \mathbf{x}) = \sum_{k=1}^s \mathbf{J}^k = \sum_{k=1}^s q^k \int_{\mathbb{R}^3} \mathbf{v} f^k(t, \mathbf{x}, \mathbf{v}) d\mathbf{v}. \quad (5.20)$$

The momentum and temperature of the k -th particle are defined as

$$\rho^k \mathbf{u}^k = q_k \int_{\mathbb{R}^3} \mathbf{v} f^k d\mathbf{v}, \quad \rho^k |\mathbf{u}^k|^2 + 3\rho^k \mathcal{T}^k = q_k \int_{\mathbb{R}^3} |\mathbf{v}|^2 f^k d\mathbf{v}. \quad (5.21)$$

In this multi-particle model, the discretized total energy, electric energy, magnetic energy, and kinetic energy of the system at time t^n are defined as

$$\mathcal{E}_{\text{total},h}^n = \sum_{k=1}^s (\mathcal{E}_{K,h}^k)^n + \mathcal{E}_{E,h}^n + \mathcal{E}_{B,h}^n, \quad (5.22)$$

with

$$(\mathcal{E}_{K,h}^k)^n = \frac{1}{2} \sum_{j \in J} \Delta V (\rho_j^k)^n [|\mathbf{u}_j^n|^2 + 3(\mathcal{T}_j^k)^n]. \quad (5.23)$$

Remark 2. The normalization of the multi-particle VM system (5.17), (5.18) and (5.19) is similar to [21]. The elementary charge e and the electron mass m^e are treated as standard charge and mass, respectively. ϵ_0 is the permittivity of the vacuum, while n_0 is a reference electron density. Then, the normalization is done as below

$$\hat{t} = \frac{t}{1/\omega_{\text{pe}}}, \quad \hat{\mathbf{v}} = \frac{\mathbf{v}}{c}, \quad \hat{\mathbf{x}} = \frac{\mathbf{x}}{L_0}, \quad \hat{\mathbf{B}} = \frac{\mathbf{B}}{B_0}, \quad \hat{\mathbf{E}} = \frac{\mathbf{E}}{cB_0}, \quad (5.24)$$

where $\omega_{\text{pe}} = \sqrt{\frac{e^2 n_0}{\epsilon_0 m^e}}$, and c is the speed of light. The inertial length of the electron $L_0 = c/\omega_{\text{pe}}$. Finally, we could derive the cyclotron frequency of species k as $\omega_{\text{ck}} = eB_0/m^k$.

For the Orszag-Tang vortex problem, the initial condition is as follows, and we refer [21, 25] for more details.

$$f^k(0, \mathbf{x}, \mathbf{v}) = \frac{n^k}{(2\pi\mathcal{T}^k)^{3/2}} \exp\left(-\frac{|\mathbf{v} - \mathbf{U}^k|^2}{2\mathcal{T}^k}\right), \quad (\mathbf{x}, \mathbf{v}) \in [0, L]^2 \times \mathbb{R}^3, \quad k = i, e, \quad (5.25)$$

with

$$\begin{aligned} n^k &= \gamma^2, & \mathbf{U}^k &= [-\bar{B}\bar{v} \sin(y), \bar{B}\bar{v} \sin(x), 0], & k &= i, e, \\ \mathbf{E} &= \mathbf{0}, & \mathbf{B} &= [0, \bar{B} \sin(2x), 0], & \mathcal{T}^i &= 0.024, & \mathcal{T}^e &= 0.6. \end{aligned} \quad (5.26)$$

Here, the exact values of the parameters are set as

$$\frac{m^i}{m^e} = 25, \quad \frac{\omega_{\text{pe}}}{\omega_{\text{ce}}} = 1, \quad \gamma = 5/3, \quad L = 2\pi, \quad \bar{B} = 0.5, \quad \bar{v} = 0.5. \quad (5.27)$$

Moreover, pressure P^k is defined as

$$P^k = \rho^k \mathcal{T}^k = m^k n^k \mathcal{T}^k, \quad k = i, e. \quad (5.28)$$

Since this is a 2D3V problem, which is quite expensive to simulate, we set the mesh number as $N_x = N_y = 100$ with linear reconstruction utilized in the spatial space, and the moment number is set as $M = 30$. For the MHD problem, people are usually interested in the multiples of Alfvén time $t_{\text{Alfvén}} = L_0/\bar{v}$, where L_0 equals 1 in the normalized system (5.17) [20]. In this test, the final simulation time is set as $t = 2t_{\text{Alfvén}} = 4$. The evolution of electric energy $\mathcal{E}_{E,h}^n$, magnetic energy $\mathcal{E}_{B,h}^n$, and kinetic energy $\mathcal{E}_{K,h}^s$, $s = i, e$ is shown in Fig. 11(a), where the reference solution obtained by DVM is also plotted. Fig. 11(a) shows that for the evolution of each energy, the numerical solution fits well with the reference solution. Fig. 11(b) illustrates the variation of the relative error for the total energy. We can find that for this complicated

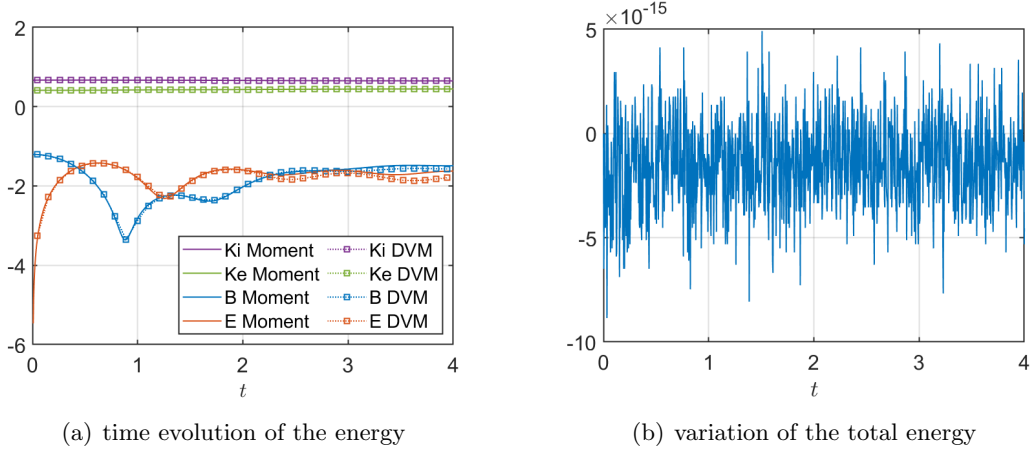


Figure 11: (Sec. 5.4) (a) Time evolution of the electromagnetic field energy and kinetic energy of ions and electrons defined in (5.23). Here, the x -axis is time t , and the y -axis is logarithmic form of the corresponding energy $\log_{10}(\mathcal{S}/L^2)$, $\mathcal{S} = \mathcal{E}_{B,h}^n, \mathcal{E}_{E,h}^n, (\mathcal{E}_{K,h}^k)^n, k = i, e$. (b) Time variation of the relative error for the total energy as $V(\mathcal{E}_{\text{total},h}^n)$ defined as (5.8). Here, the x -axis is time t , and the y -axis is $V(\mathcal{E}_{\text{total},h}^n)$.

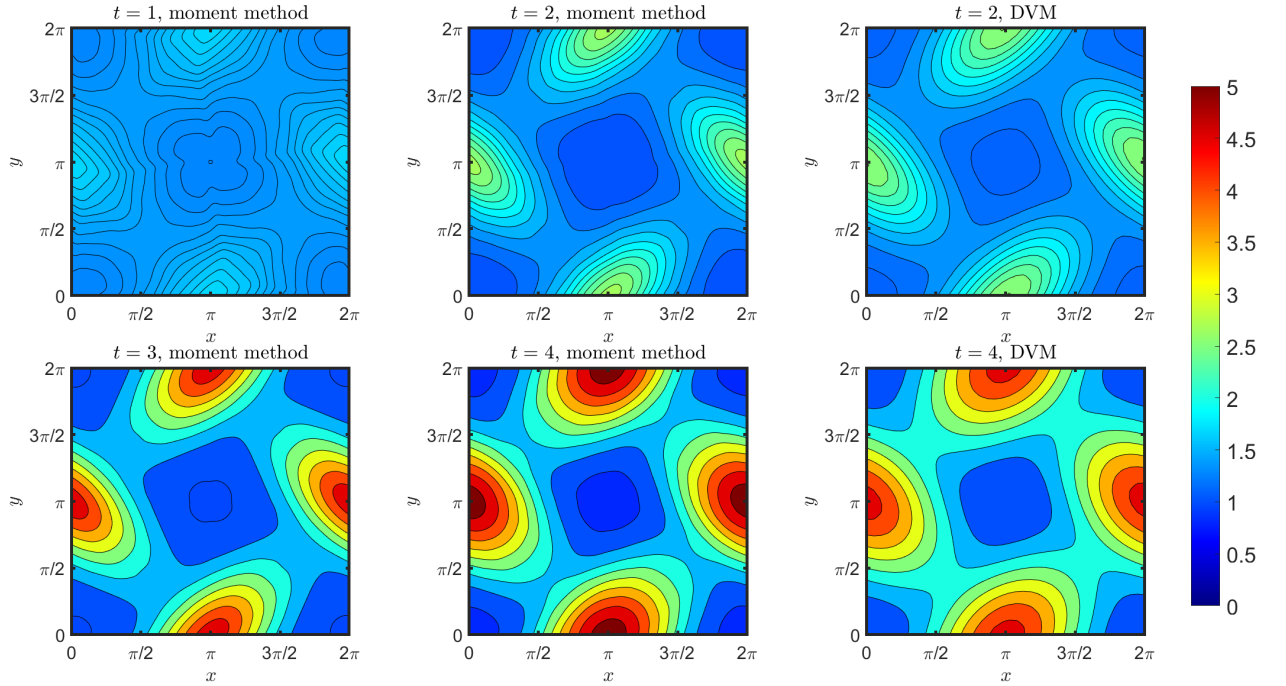


Figure 12: (Sec. 12) The pressure for the ion $P^i = m^i \rho^i \mathcal{T}^i$ at $t = 1, 2, 3$ and 4 . The left two columns are those by the moment method and the right column is the reference solution by DVM.

2D3V example with multi-particles, this regularized moment method could still preserve the conservation of the total energy well.

Fig. 12 shows the pressure distribution diagram of the ions at different time, and the reference pressure at $t = 2$ and 4 is also plotted. At first, the pressure is uniform and small vortices start to form gradually. At $t = 2t_{\text{Alfvén}} = 4$, there are almost four vortices, and the numerical results are consistent with the reference solution. In the Orszag-Tang vortex example,

people are always interested in density ρ and current J_z . The density ρ^i and the current of the ions $J_z^i = q^i m^i u_z^i$ at time $t = 1, 2, 3$ and 4 are illustrated in Fig. 13 and 14, respectively. The evolution of ρ^i is similar to that of pressure P^i , which is uniform at the beginning, and four vertices form at $t = 4$. For the current, it is also smooth at the beginning, and evolves to several vortices and oscillations with time going.

The time evolution of the magnetic field is shown in Fig. 15, where the same color interval is utilized for all figures. The background is the total magnetic energy, and the white arrow lines are the magnetic fields. At the initial time as in Fig. 15(a), the magnetic field has four peaks, forming four uniform magnetic field bands on the xy -plane. Then, the peak value gradually decreases, but the direction of the magnetic field is barely changed in Fig. 15(b). In Fig. 15(c) and 15(d), the global magnetic energy becomes quite small, and each band is distorted, with two peaks forming. Then, two peaks at the center of the xy -plane and four peaks at the four corners appear in Fig. 15(e) and 15(f). Finally, the magnetic field lines are beginning to twist in Fig. 15(g). At $t = 4$, the double peaks in the center merge to one peak, and the five peaks are growing larger and larger in Fig. 15(i). From Fig. 15, we could clearly see the variation of the magnetic field, and more complicated phenomenon will appear with time going, which will be left for future work.

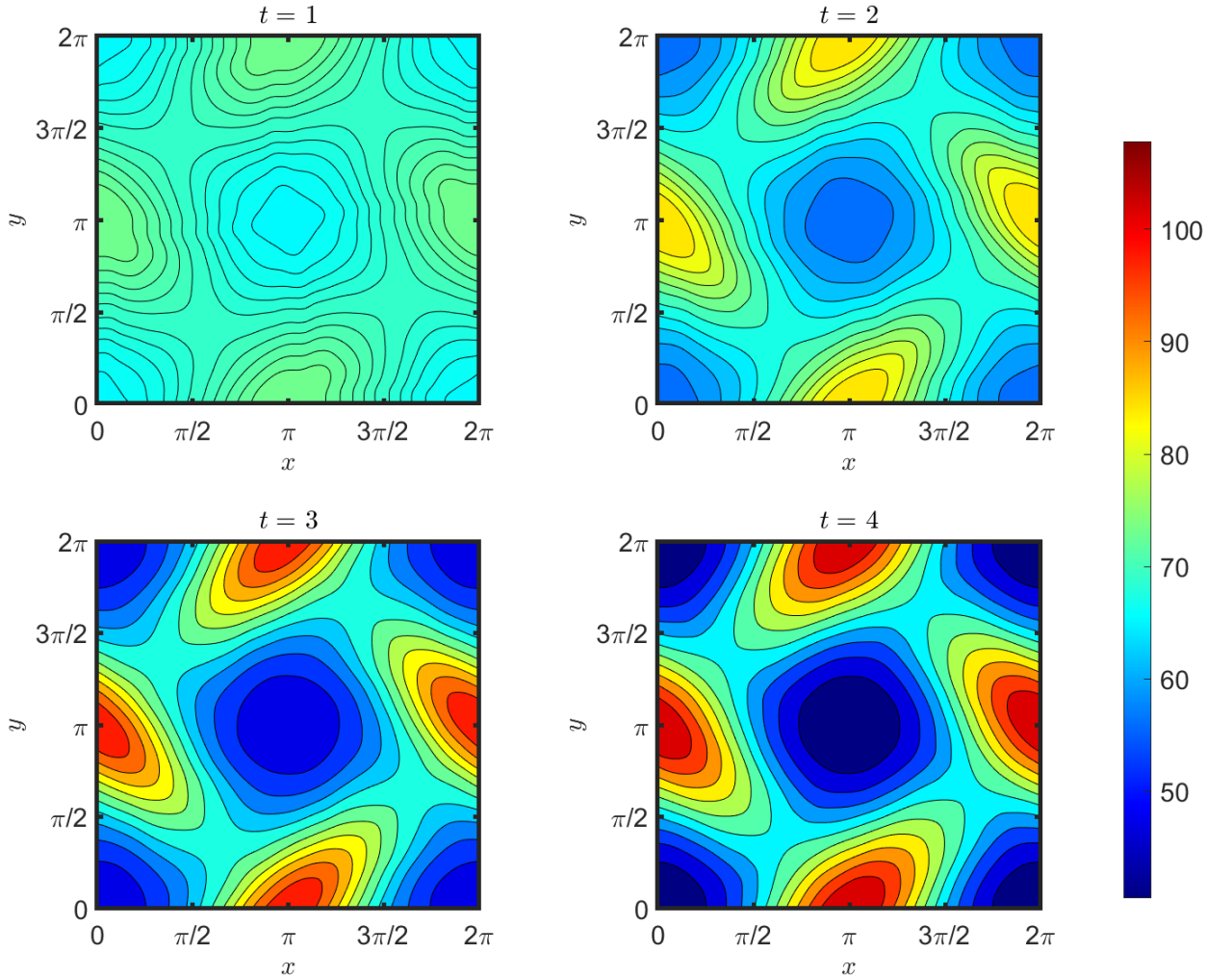


Figure 13: (Sec. 5.4) The density of the ions ρ^i at $t = 1, 2, 3$ and 4.

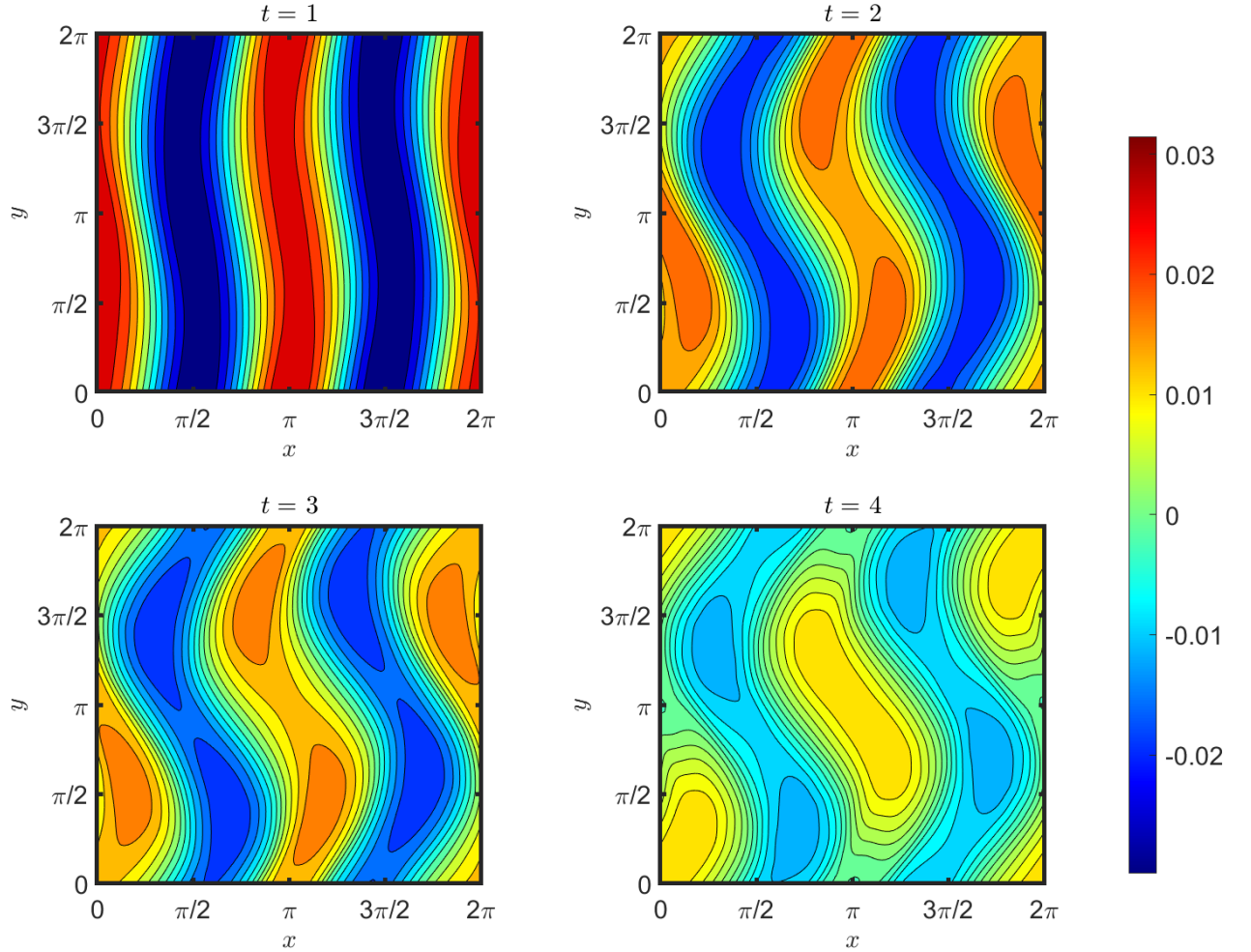


Figure 14: (Sec. 5.4) The current density of ions J_z^i at $t = 1, 2, 3$ and 4 .

6 Conclusion

In this paper, the globally hyperbolic moment system is derived for the VM system under the framework of the Hermite spectral method. With the expansion center chosen as the local macroscopic velocity and the scaling factor as the temperature, the movement of the particles led by the Lorentz force can be expressed with the linear combination of the moment coefficients. Therefore, only quite a few degrees of freedom are needed to describe the effect of the Lorentz force. An energy-preserving numerical scheme for the moment system, where only a small linear equation system needs to be solved, is proposed. The numerical results of Landau damping, two-stream instability, Weibel instability, and Orszag-Tang vortex problems are shown to verify the efficiency and energy-preserving ability of this numerical scheme.

It is illustrated that the globally hyperbolic moment system is a promising alternative to model the VM system. The numerical scheme with large time step and more applications will be studied in the future.

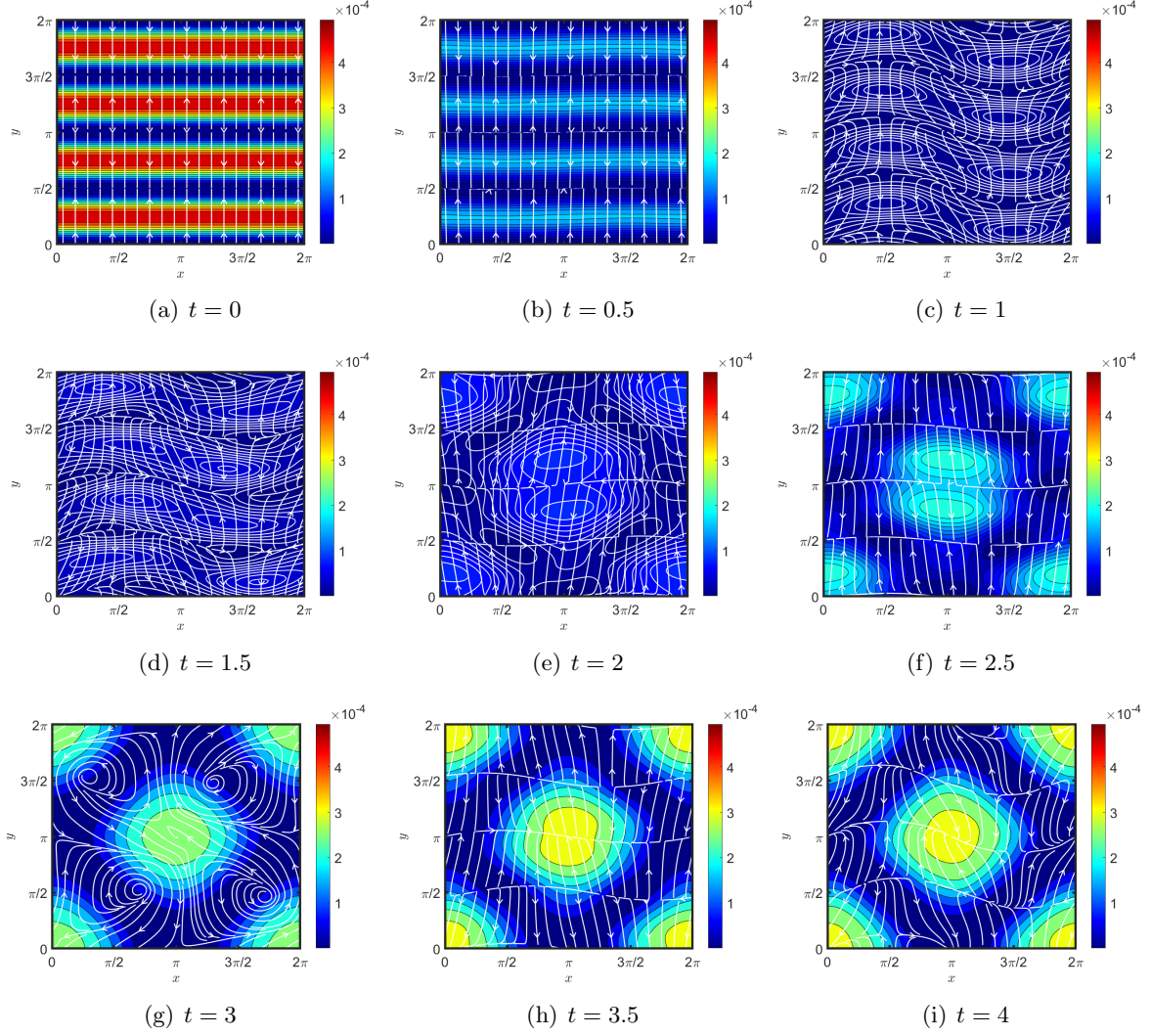


Figure 15: (Sec. 5.4) Time evolution of the magnetic field. Here, the background is the total magnetic energy, and the white line is the magnetic field.

Acknowledgements

We thank Prof. Ruo Li from PKU, Prof. Zhenning Cai from NUS for their valuable suggestions. Xinghui Zhong is partially supported by the National Natural Science Foundation of China (Grant No. 11871428). The work of Yanli Wang is partially supported by the National Natural Science Foundation of China (Grant No. 12171026, U1930402 and 12031013).

References

- [1] C.K. Birdsall and A.B. Langdon. *Plasma physics via computer simulation*. CRC press, 2018.
- [2] J.A. Bittencourt. *Fundamentals of plasma physics*. Springer Science & Business Media, 2013.
- [3] X. Cai, S. Boscarino, and J. Qiu. High order semi-Lagrangian discontinuous Galerkin method coupled with Runge-Kutta exponential integrators for nonlinear Vlasov dynamics. *Journal of Computational Physics*, 427:110036, 2021.

- [4] Z. Cai, Y. Fan, and R. Li. Globally hyperbolic regularization of Grad’s moment system. *Communications on pure and applied mathematics*, 67(3):464–518, 2014.
- [5] Z. Cai, R. Li, and Y. Wang. Solving Vlasov equations using NRxx method. *SIAM Journal on Scientific Computing*, 35(6):A2807–A2831, 2012.
- [6] F. Califano, N. Attico, F. Pegoraro, G. Bertin, and S.V. Bulanov. Kinetic saturation of the Weibel instability in a collisionless plasma. *Physical Review E*, 57(6):7048, 1998.
- [7] F. Califano, N. Attico, F. Pegoraro, G. Bertin, and S.V. Bulanov. Fast formation of magnetic islands in a plasma in the presence of counterstreaming electrons. *Physical Review Letters*, 86(23):5293, 2001.
- [8] G. Chen, L. Chacón, and D.C. Barnes. An energy- and charge-conserving, implicit, electrostatic Particle-in-Cell algorithm. *Journal of Computational Physics*, 230(18):7018–7036, 2011.
- [9] Y. Cheng, A.J. Christlieb, and X. Zhong. Energy-conserving discontinuous Galerkin methods for the Vlasov-Ampère system. *Journal of Computational Physics*, 256, 2013.
- [10] Y. Cheng, A.J. Christlieb, and X. Zhong. Energy-conserving discontinuous Galerkin methods for the Vlasov-Maxwell system. *Journal of Computational Physics*, 256(1):630–655, 2014.
- [11] Y. Cheng, I.M. Gamba, F. Li, and P.J. Morrison. Discontinuous Galerkin methods for the Vlasov-Maxwell equations. *SIAM Journal on Numerical Analysis*, 52(2):1017–1049, 2014.
- [12] N. Crouseilles, L. Einkemmer, and E. Faou. Hamiltonian splitting for the Vlasov–Maxwell equations. *Journal of Computational Physics*, 283:224–240, 2015.
- [13] J. Dawson. One-dimensional plasma model. *The Physics of Fluids*, 5(4):445–459, 1962.
- [14] F. Doveil, D.F. Escande, and A. Macor. Experimental observation of nonlinear synchronization due to a single wave. *Physical Review Letters*, 94(8):085003, 2005.
- [15] R. Duclous, B. Dubroca, F. Filbet, and V. Tikhonchuk. High order resolution of the Maxwell-Fokker-Planck-Landau model intended for ICF applications. *Journal of Computational Physics*, 228(14):5072–5100, 2009.
- [16] L. Einkemmer and I. Joseph. A mass, momentum, and energy conservative dynamical low-rank scheme for the Vlasov equation. *Journal of Computational Physics*, 443:110495, 2021.
- [17] B. Eliasson. Numerical modelling of the two-dimensional Fourier transformed Vlasov-Maxwell system. *Journal of Computational Physics*, 190(2):501–522, 2003.
- [18] E.G. Evstatiev and B.A. Shadwick. Variational formulation of particle algorithms for kinetic plasma simulations. *Journal of Computational Physics*, 245:376–398, 2013.
- [19] J.D. Jackson. *Classical electrodynamics*, volume 31999. Wiley New York, 1977.
- [20] H. Kigure, K. Takahashi, K. Shibata, T. Yokoyama, and S. Nozawa. Generation of Alfvén waves by magnetic reconnection. *Publications of the Astronomical Society of Japan*, 62(4):993–1004, 2010.
- [21] O. Koshkarov, G. Manzini, G.L. Delzanno, C. Pagliantini, and V. Roytershteyn. The multi-dimensional Hermite-discontinuous Galerkin method for the Vlasov-Maxwell equations. *Computer Physics Communications*, 264:107866, 2021.

- [22] N.A. Krall and A.W. Trivelpiece. Principles of plasma physics. *American Journal of Physics*, 41(12):1380–1381, 1973.
- [23] L.D. Landau. On the vibrations of the electronic plasma. *The Collected Papers of LD Landau*, pages 445–460, 1965.
- [24] H.R. Lewis. Energy-conserving numerical approximations for Vlasov plasmas. *Journal of Computational Physics*, 6(1):136–141, 1970.
- [25] C. Liu and K. Xu. Unified gas-kinetic wave-particle methods IV: multi-species gas mixture and plasma transport. *Advances in Aerodynamics*, 3(9), 2011.
- [26] J.H. Malmberg and C.B. Wharton. Collisionless damping of electrostatic plasma waves. *Physical Review Letters*, 13(6):184, 1964.
- [27] S. Markidis and G. Lapenta. The energy conserving Particle-in-Cell method. *Journal of Computational Physics*, 230(18):7037–7052, 2011.
- [28] P.J. Morrison. The Maxwell-Vlasov equations as a continuous Hamiltonian system. *Physics Letters A*, 80(5-6):383–386, 1980.
- [29] P.J. Morrison. A general theory for gauge-free lifting. *Physics of Plasmas*, 20(1):012104, 2013.
- [30] C. Nicolas and F. Francis. Numerical approximation of collisional plasmas by high order methods. *Journal of Computational Physics*, 201(2):546–572, 2004.
- [31] C. Pagliantini, G. Manzini, O. Koshkarov, G.L. Delzanno, and V. Roytershteyn. Energy-conserving explicit and implicit time integration methods for the multi-dimensional Hermite-DG discretization of the Vlasov-Maxwell equations. *arXiv preprint arXiv:2110.11511*, 2021.
- [32] T.N. Parashar, S. Servidio, M.A. Shay, W.H. Matthaeus, and P.A. Cassak. Orszag Tang vortex–Kinetic study of a turbulent plasma. In *AIP Conference Proceedings*, volume 1216, pages 304–307. American Institute of Physics, 2010.
- [33] J. Qiu and A. Christlieb. A conservative high order semi-Lagrangian WENO method for the Vlasov equation. *Journal of Computational Physics*, 229(4):1130–1149, 2010.
- [34] J. Qiu and C. Shu. Conservative high order semi-Lagrangian finite difference WENO methods for advection in incompressible flow. *Journal of Computational Physics*, 230(4):863–889, 2011.
- [35] J. Qiu and C. Shu. Positivity preserving semi-Lagrangian discontinuous Galerkin formulation: theoretical analysis and application to the Vlasov-Poisson system. *Journal of Computational Physics*, 230(23):8386–8409, 2011.
- [36] T.H. Stix. *Waves in plasmas*. Springer Science & Business Media, 1992.
- [37] H. Struchtrup. Macroscopic transport equations for rarefied gas flows. In *Macroscopic transport equations for rarefied gas flows*, pages 145–160. Springer, 2005.
- [38] D. Tskhakaya, K. Matyash, R. Schneider, and F. Taccogna. The Particle-in-Cell method. *Contributions to Plasma Physics*, 47(8-9):563–594, 2007.
- [39] T. Umeda, K. Togano, and T. Ogino. Two-dimensional full-electromagnetic Vlasov code with conservative scheme and its application to magnetic reconnection. *Computer Physics Communications*, 180(3):365–374, 2009.

- [40] Y. Wang and S. Zhang. Solving Vlasov-Poisson-Fokker-Planck equations using NRxx method. *Communications in Computational Physics*, 21(3):782–807, 2017.
- [41] N. Zheng, X. Cai, J. Qiu, and J. Qiu. A conservative semi-Lagrangian hybrid Hermite WENO scheme for linear transport equations and the nonlinear Vlasov-Poisson system. *SIAM Journal on Scientific Computing*, 43:3580–3606, 2021.